ADVANCED FUNCTIONAL MATERIALS
www.afm-journal.de

Structure and Properties of Prussian Blue Analogues in Energy Storage and Conversion Applications

Haocong Yi, Runzhi Qin, Shouxiang Ding, Yuetao Wang, Shunning Li, Qinghe Zhao, and Feng Pan**

In recent years, Prussian blue analogue (PBA) materials have been widely explored and investigated in energy storage/conversion fields. Herein, the structure/property correlations of PBA materials as host frameworks for various charge-carrier ions (e.g., Na^+, K^+, Zn^{2+}, Mg^{2+}, Ca^{2+}, and Al^{3+}) is reviewed, and the optimization strategies to achieve advanced performance of PBA electrodes are highlighted. Prospects for further applications of PBA materials in proton, ammonium-ion, and multivalent-ion batteries are summarized, with extra attention given to the selection of anode materials and electrolytes for practical implementation. This work provides a comprehensive understanding of PBA materials, and will serve as a guidance for future research and development of PBA electrodes.

1. Introduction

As typical metal–organic framework materials, Prussian blue analogues (PBAs) have long been studied and applied in various fields. They were first synthesized in Berlin as pure synthetic pigments in the early 18th century.[1] Subsequently, with the development of science and technology, as well as gradually deepening understanding of PBA materials, many other applications were developed, including gas storage,[2–5] environmental purification,[6–8] drug delivery,[9–12] etc., mainly due to their high porosity character. In addition, they not only displayed high activity as an efficient water oxidation catalyst,[13] but can also be utilized as the biosensors to measure hydrogen peroxide, glucose, lactic acid, cholesterol,[14–15] and etc. In the last decade, research on PBA materials was focused on their potential utility as cathode materials in various kind of secondary batteries.

PBAs can display several advantages when used as energy storage materials: i) the open framework of PBAs provides abundant 3D diffusion channels for diffusion of various charge-carrier ions;[16,17] ii) compositional control in PBAs regarding the transition metal ions can be achieved for optimizing the charge storage behavior of PBAs with negligible change in the overall open framework structure;[18] iii) the tough open framework structure of PBA materials results in a high cycling stability of PBA-based electrodes;[19] and iv) the low-cost PBAs are suitable for large-scale energy storage applications. Thus, in 1978, Neff et al.[20,21] first reported the electrochemical behavior of an electrodeposited PBA material on platinum foil as a host framework for the reversible insertion/extraction of K^+ ions (and/or other hydrated ions) in aqueous solutions. In 1999, the reversible charge storage of Li^+ in PBA materials was also reported in organic solvents.[22,23] These early attempts were only marginally successful due to the serious capacity fading problems that PBAs suffer from.[24,25] In the last decade, due to the development of energy storage technology and the imperious demand for low-cost electrode materials, researchers once again set their sights on PBA materials.[26] For instance, in 2011, Cui's group[27] evaluated $KCu[Fe(CN)_6]$ as cathode in aqueous K^+-ion batteries, which presented a high cycle stability with capacity retention of 83% in 40 000 cycles. Furthermore, the mass loading of PBA active materials was also increased to 10 mg cm^{-2}, which met the requirements in the practical battery applications.[28] Goodenough et al.[29] synthesized a series of PBA materials with different N coordinated transition metals as potential cathodes in Na^+-ion batteries, which achieved a flat discharge capacity of >70 mAh g^{-1}, as well as good reversibility. Recently, various kinds of PBAs have been developed as cathodes in Na^+-ion and K^+-ion batteries.[30] Besides, the applications of PBA materials as cathodes in supercapacitors have also been disclosed, such as $GdCo(CN)_6$ for Li^+-ion storage,[31] $CoHCF/MnO_2$[32] and $K_{1.7}Na_{0.27}Co[Fe(CN)_6]_{0.71}\cdot 1.6H_2O$[33] for Na^+-ion storage, etc. It is worth noting that Huang's group have conducted systematic works on K^+-ion storage of PBA materials in supercapacitors, in which the MnHCF,[34] Fe-HCF,[35] and $Mn_3[Co(CN)_6]_2\cdot nH_2O$[36] were successively applied as cathodes and exhibited high capacitance and excellent cycling performance.

Researchers have also explored the possible applications of PBA materials for charge storage of multivalent ions, including Zn^{2+}, Mg^{2+}, Ca^{2+}, and Al^{3+} ions. In 2013, Okubo et al.[37] reported the reversible intercalation of Mg^{2+} into CuFe-PBA in aqueous electrolytes. Simultaneously, Cui et al.[38] reported that a series of alkaline earth metal divalent ions in aqueous electrolytes (Mg^{2+}, Ca^{2+}, Sr^{2+}, Ba^{2+}) can be reversibly intercalated in the nanolevel NiHCF electrode, showing excellent cycle and rate performances. Gao et al.[39] and Chiang

H. Yi, Dr. R. Qin, S. Ding, Y. Wang, Dr. S. Li, Dr. Q. Zhao, Prof. F. Pan
School of Advanced Materials
Peking University Shenzhen Graduate School
Shenzhen 518055, P. R. China
E-mail: zhaoqh@pku.edu.cn; panfeng@pkusz.edu.cn

The ORCID identification number(s) for the author(s) of this article can be found under https://doi.org/10.1002/adfm.202006970.

DOI: 10.1002/adfm.202006970

et al.[40] reported the reversible intercalation of Al^{3+} into CuFe-HCF cathodes in secondary batteries and capacitors, respectively. Ingram et al.[41] also reported the reversible insertion and release of calcium (Ca^{2+}) ions in manganese ferricyanide (MnHCF), which is the first report on the reversible intercalation/extraction of divalent cations in PBAs in a non-aqueous electrolyte system. Moreover, the diffusion/storage of Zn^{2+} ions in PBA materials was explored. For example, Mantia et al.[42] and Liu et al.[43] reported the electrochemical performances of CuHCF and ZnHCF as cathodes in the aqueous zinc-ion batteries, respectively, which showed a high discharge platform up to 1.7 V, as well as an excellent cycle stability.

The above reports indicated a wide feasibility of PBA materials for various carrier ions, including both the monovalent ions (NH_4^+, Li^+, Na^+, and K^+) and multivalent ions (Zn^{2+}, Mg^{2+}, Ca^{2+}, and Al^{3+}), mainly due to their open frameworks. However, there are still some challenges for the further development of PBA materials, which restrict their practical applications: i) the irreversible phase transition of PBA materials occurs during deep discharge/charge process; ii) the $[Fe(CN)_6]$ vacancies and coordinated water in the crystal framework of PBA materials reduce the crystallinity, leading to the loss in capacity retention and cycle life;[19] iii) side reactions (oxygen evolution reactions) exist due to the narrow electrochemical window of aqueous electrolytes;[44] iv) the electrochemical reaction mechanisms of the PBA cathodes is complicated and differs in correspondence to the variation of intercalating ion species, PBA compositions, as well as electrolyte systems.

Recently, several review/progress on the research of PBAs have been conducted, among which some works focused mainly on applications of PBAs in alkaline-ion batteries and electrochemical catalysts,[19,45,46] while others on either the electrochemical performances of PBAs-derived materials[47,48] or their crystal structure, synthesis, and working principle in rechargeable batteries.[30,49] In this work, differing from the previous reviews, we present a novel perspective on the potential application of PBAs and the strategies to optimize them in future energy storage/conversion technologies, after making a detailed summary of the crystal structure and reaction mechanisms of the PBA-based host materials (**Figure 1**). Specifically, the proposed optimization strategies provide some basic and practical methods for promoting PBA electrode performances, including reducing crystal vacancies and crystal water, metal-doping control, constructing concentration gradient and core–shell structure, designing novel morphology, developing PBA-based composite materials, and applying high-concentration electrolytes. Additionally, prospects for further applications of PBA materials in proton, ammonium-ion, and multivalent-ion batteries are discussed, with extra attention given to the selection of anode materials and electrolytes for practical implementation. This work provides a comprehensive understanding of PBA materials, and will shed light on the future research and development of PBA electrodes.

2. Crystal Structure of PBA Materials

The electrochemical performance of electrodes is closely related to their structures.[50] The basic Prussian blue (PB)

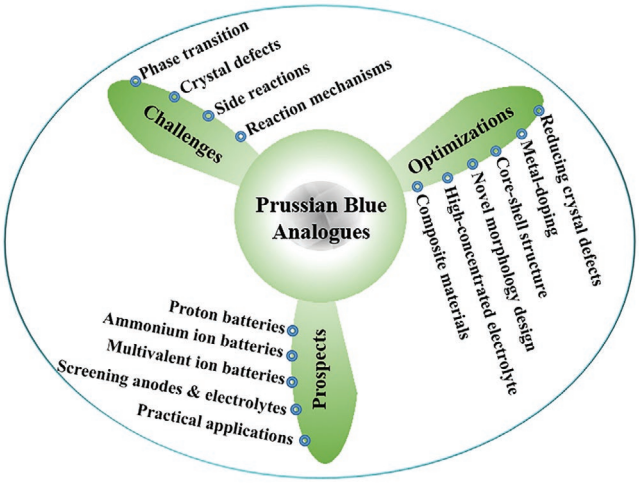

Figure 1. Schematic illustration of the challenges, optimizations, and prospects of PBA materials in energy storage/conversion applications.

material, $Fe_4[Fe(CN)_6]_3 \cdot nH_2O$, has a face-centered cubic phase with a *Fm*3*m* space group. The detailed structure of $Fe_4[Fe(CN)_6]_3 \cdot nH_2O$ has been detected through X-ray diffraction and neutron diffraction analysis.[51–53] Divalent and trivalent Fe atoms appear alternately in the face-centered cubic structure connecting with the −C≡N− bonds. Among them, Fe^{2+} and Fe^{3+} ions are surrounded by C and N to form octahedrons, respectively. In order to maintain electrical neutrality, the Fe^{2+}: Fe^{3+} ratio is maintained at about ≈3:4. As a result, there exist ≈25% vacancies in the $[Fe(CN)_6]^{4-}$ sites, which will be filled by water molecules. Two types of the structural water molecules are present in the structure of PB: one is coordinated water in the empty nitrogen sites with six water molecules coordinated to Fe(III), and the other contains up to 8 interstitial water which either fill in the center of the unit cell or connect with the hydrogen bonds to the coordinated ones. Therefore, a single PB unit cell may contain up to 14 water molecules. The interstitial water in PBA materials can strongly affect the electrochemical performance. For example, Wu et al.[54] reported that the Fe and Mn redox in hydrated $Na_xMnFe(CN)_6 \cdot zH_2O$ electrodes are separated with different potentials, while a mixed Fe and Mn redox in the same potential range is found in the anhydrated $Na_xMnFe(CN)_6$ electrode. Adding the interstitial water weakens the ligand field stabilization energy of low-spin Fe^{2+} and high-spin Mn^{2+} by diluting the ligand field and increasing the lattice constant, leading to re-emergence of the gap between the $Fe^{2+/3+}$ and $Mn^{2+/3+}$ redox potentials.

The crystal structure of the PBA materials can be tuned via changing the chemical composition of PBA materials.[46] Generally, there exist three types of crystal structures for PBA materials, i.e., cubic-type (e.g., $K_xFe_yMn_{1-y}[Fe(CN)_6]_w \cdot zH_2O$[55]), monoclinic-type (e.g., $Na_{1.96}Mn[Mn(CN)_6]_{0.99-\Upsilon 0.01} \cdot 2H_2O$[56]), and rhombohedral-type (e.g., $Na_2Mn[Fe(CN)_6] \cdot zH_2O$[57]) structures. PBA materials possess the chemical formula of $A_xP[R(CN)_6]_{1-y}\ \Upsilon_y \cdot nH_2O$ (where A = alkali metal or alkaline earth metal, P and R represent the transition metals, Υ is the $[R(CN)_6]$ vacancies, and $0 \le x \le 2$, $y < 1$), in which the nitrogen-coordinated P cations and carbon-coordinated R cations in an open framework bridged by cyanide groups (−C≡N−)[56]

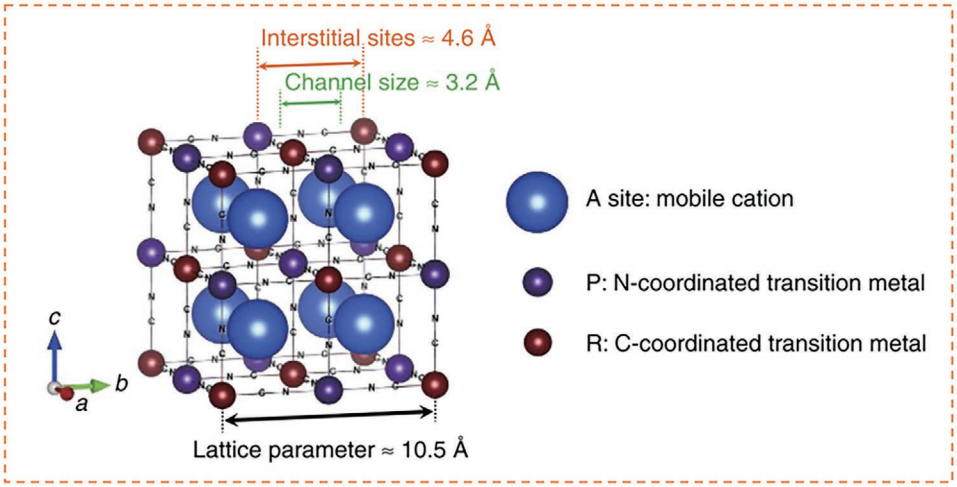

Figure 2. Schematic illustrations of $A_xP[R(CN)_6]_y{\cdot}nH_2O$ materials (A is the alkali metal or alkaline earth metal, P and R represent transition metals in different locations, and $0 \le x \le 2$, $y < 1$. Reproduced with permission.[56] Copyright 2014, Springer Nature.

(**Figure 2**). The alkali metal ions or alkaline earth metal ions (A) are usually inserted into the 8c site, while the transition metals (P, R) replace the $Fe^{2+/3+}$ sites. Thus, various kinds of PBA materials have been developed with optimized electronic and ionic properties for enhancing the electrode performance. The open-framework nature of PBA structures, which contain open <100> channels (3.2 Å in diameter) and interstitial sizes (4.6 Å in diameter) enabling rapid solid-state diffusion of various carrier ions. The electrode capacity is contributed by the electrochemical redox reactions of the transition metal ions in either the P or R sites, that is to say, both the N-coordinated and C-coordinated transition metals can be electrochemically active. Taking the monovalent A^+ as an example, in a vacancy-free PBA electrode, the redox reaction is as follow

$$P\left[R(CN)_6\right] + xA^+ + xe^- \leftrightarrow A_xP\left[R(CN)_6\right] \quad (1)$$

Apparently, the PBA framework structure exhibit abundant wide channels for insertion/extraction of carrier ions in A sites (along <100> directions), in both aqueous and nonaqueous electrolytes.

3. Electrode Reaction Mechanisms

Revealing the electrochemical reaction mechanisms during charge/discharge process is of great importance to develop advanced electrode materials,[58–60] and the crystal and electronic structures of electrodes can be detected by many methods, including in situ/ex situ X-ray diffractions (XRD),[61,62] transmission electron microscopy (TEM),[63,64] soft X-ray spectroscopy (SXS),[65] etc. For PBA materials, the open frameworks provide numerous 3D tunnels for intercalating various carrier ions.[30,66] Pasta et al.[67] studied the structural properties of MnHCF/CoHCF as hosts for Na^+ ion storage in an aqueous $NaClO_4$ electrolyte. They found that the C-coordinated Fe plays a role of preserving the crystal structure and enabling the outstanding kinetics and cycle life. Meanwhile, although the N-coordinated Co/Mn ions contribute significantly toward increasing the electrode capacity delivery, a slower reaction kinetic induced by the structural distortions from the weak N-coordinated crystal field was detected. Reducing this kind of structural distortions during charge/discharge process will benefit for the long-term cycling stability. Xie et al.[68] revealed that Ni^{2+} in NiHCF can effectively reinforce the lattice framework by alleviating the alterations of cell volume and stress–strain caused by Na^+ ion migration and structure transition. Furthermore, Lee et al.[69] reported that the inserted ion species and applied electrolyte also play a vital role on the electrochemical reactions of PBAs. The authors showed that NiHCF structure offers fast solid-state diffusion of Li^+, Na^+, and K^+ ions in aqueous electrolytes, while exhibiting only a quasi-reversible electrochemical behavior for all alkali ions in organic electrolytes and Rb^+ and Cs^+ in aqueous electrolytes.

The reversible structure evolution of PBA materials for monovalent ions intercalation have been intensively reported, including $Na_2Ni_{0.4}Co_{0.6}[Fe(CN)_6]$,[70] $K_2Zn_3(Fe(CN)_6)_2 \cdot 9H_2O$,[71] $K_{0.6}Ni_{1.2}Fe(CN)_6 \cdot 3.6H_2O$,[28] etc. For instance, Jiang et al.[55] investigated the K^+ ion intercalation behavior in $K_xFe_yMn_{1-y}[Fe(CN)_6]_w \cdot zH_2O$ samples (monoclinic, space group of $P21/n$, **Figure 3**a). For $KMn[Fe(CN)_6]$ electrode, multiple-phase transitions from monoclinic to cubic and cubic to tetragonal phases were observed during charging (Figure 3b), corresponding to two voltage plateaus in the 1st cycle, with independent and symmetric Fe^{2+}/Fe^{3+}–C (0.1–1.0 V/0.9–0.0 V during the charge/discharge process) and Mn^{2+}/Mn^{3+}–N (1.0–1.3 V/1.3–0.9 V during the charge/discharge process) redox reactions. It is noted that the cubic to tetragonal phase transition reaction in high voltage can lead to the Jahn–Teller distortion of Mn^{3+} in MnN_6 octahedron during charging process, resulting on a loss in structure stability via Mn^{2+} dissolution. Fe substitution can remarkably change this Mn^{2+}/Mn^{3+}–N reaction process, and then depress the cubic to tetragonal phase transition reactions to obtain higher structure stability. For $KFe_{0.35}Mn_{0.65}[Fe(CN)_6]$ electrode, a solid solution reaction (0.4–0.95 V for charging and 0.8–0.0 V for discharging) and a phase transition reaction between monoclinic and cubic phases (0.95–1.3 V for charging and 1.3–0.8 V for discharging) were observed (Figure 3c). As a

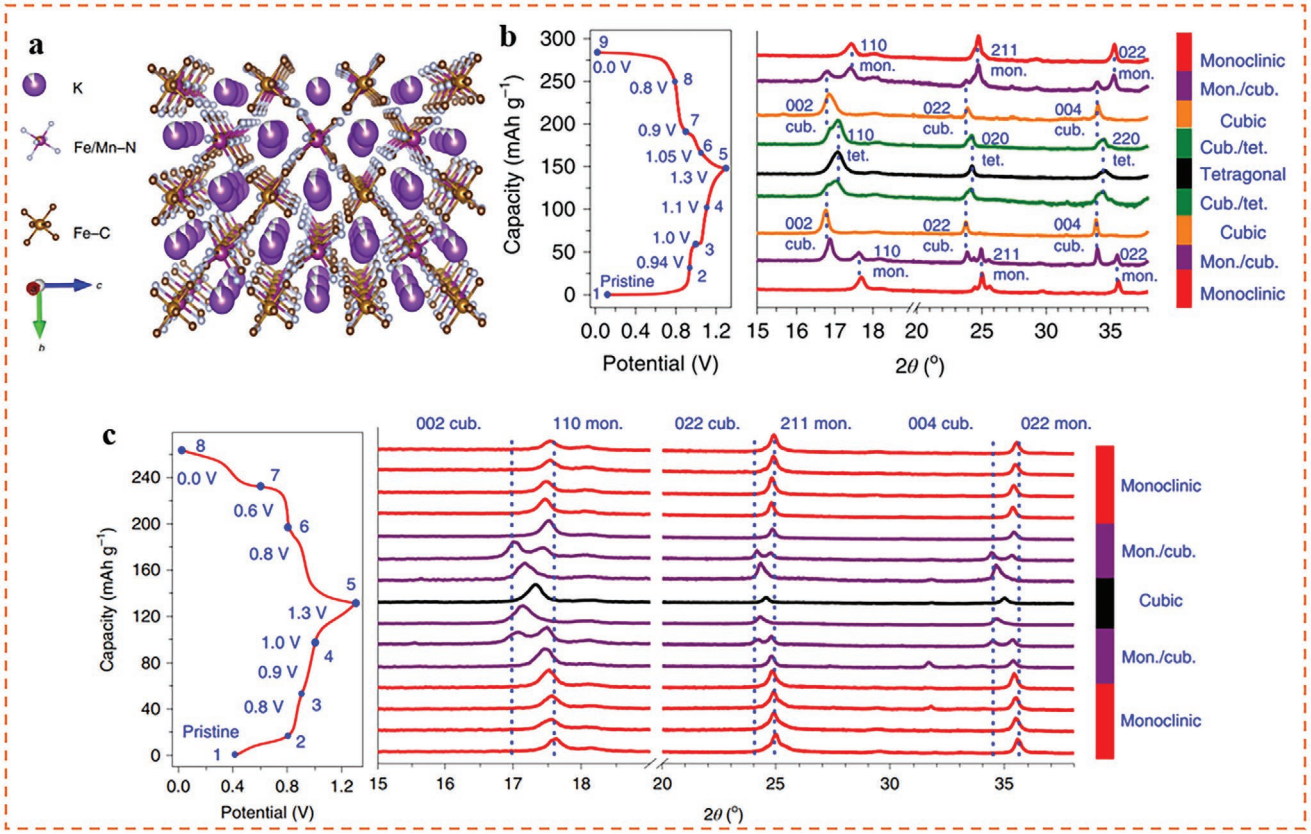

Figure 3. a) Typical structure of the KFeMnHCF in the *P*21/*n* space group, b) the structural evolution mechanism of the KMnHCF electrode, c) XRD patterns of the KFeMnHCF-3565 electrode at different states during the first cycle. Reproduced with permission.[55] Copyright 2019, Springer Nature.

result, it displayed excellent reversible K^+ storage ability, with a high cycling performance (capacity retention of 70% at 100 C rate with lifespan >10 000 cycles).

Intercalating multivalent ions in PBA materials have also attracted the interest of researchers in recent years, including NiHCF,[38] NiFeHCF,[72] $Na_2Cu_{0.6}Ni_{0.4}[Fe(CN)_6]$,[73] etc. For example, Ma et al.[74] reported the structural evolution of $KCoFe(CN)_6$ nanoparticles as host material for electrochemical Zn^{2+} storage. The $KCoFe(CN)_6$ (space group of *Fm*-3*m*) displayed a 3D cyanide-bridged architecture ($a = b = c = 10.31$ Å), with 3D porous channels to favor the Zn^{2+} ion transfer. The in situ extracting K ions from $KCoFe(CN)_6$ under galvanostatic charge produced the $CoFe(CN)_6$ as Zn^{2+}-intercalation host. The high-voltage and high-capacity of $CoFe(CN)_6$ electrode was achieved with Co^{3+}/Co^{2+}-N and subsequent Fe^{3+}/Fe^{2+}-C redox reactions upon Zn^{2+} ion insertion (in 4 M $Zn(CF_3SO_3)_2$ aqueous electrolyte) (**Figure 4**a). The potentials representing these two redox reactions located separately before cycling, then shifted gradually and finally overlap upon Zn^{2+} extraction/insertion (Figure 4b). Figure 4c shows structure evolution of $CoFe(CN)_6$ electrode during charge/discharge process via XRD pattern, in which the intensity ratio value of (011) and (200) reflections ($I_{(011)}/I_{(200)}$) decreased during discharge, and increased during charge, indicating a reversible phase transition reaction between cubic and monoclinic phases. Notably, the (011) and (200) reflections located at 17.4° and 18.4°, respectively.

Revealing the diffusion route of the carrier ions in lattice framework of the electrodes is vital for rationalizing the high-rate performance of electrode materials. Due to the 3D-tunnel feature of PBA materials, various diffusion routes of carrier ions can be demonstrated. Peng et al.[75] revealed the non-linear diffusion routes of Na^+ ions in PBA framework. Four possible Na^+ interstice sites are shown in **Figure 5**a, in which the 8c provides the largest free space while 24d offers the smallest. Figure 5b,c shows the S-shaped and linear Na^+ diffusion routes, as well as the corresponding migration energies, respectively. The results indicate that the Na^+ diffusion along an S-shaped route shows a lower energy barrier. Besides, the abundance of 24d sites in the PBA framework (20 24d sites) also guarantees the enhanced Na+ diffusion in PBA frameworks. This nonlinear Na^+ diffusion mechanism was further confirmed by Zuo's group,[68] especially when there exists interstitial water in the body-center position of the framework. To promote the diffusion kinetics in PBA materials, it is useful to employ strategies including the reduction of crystal water and metal doping control, which will be discussed in the later part.

Thus, PBA materials provide an open framework for electrochemical storage of both monovalent and multivalent ions. There usually exist multiple phase transitions (monoclinic to cubic and cubic to tetragonal phases) or two phase transition (monoclinic to cubic) during cycle, and by eliminating the cubic to tetragonal phase transition process, a high cycling stability of PBA-based electrode can be obtained, which is a very important

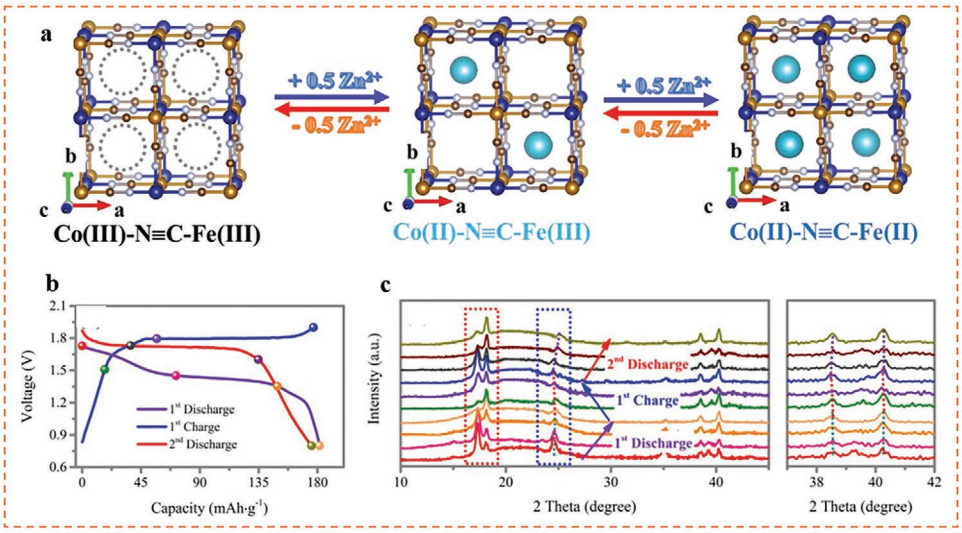

Figure 4. a) Schematic illustration of reversible Zn^{2+} storage in CoHCF frameworks during electrochemical process, b) the galvanostatic charge/discharge profile, and c) corresponding XRD patterns at selected potentials. Reproduced with permission.[74] Copyright 2019, Wiley-VCH.

index for the structural design of high-performance PBA electrode materials.

4. Electrochemical Performance

As discussed above, the chemical formula of PBA materials can be described as $A_xP[R(CN)_6]_{1-\gamma}\,\Upsilon_\gamma \cdot nH_2O$ (where A = alkali metal or alkaline earth metal, P and R represent the transition metals, Υ is the $[R(CN)_6]$ vacancies, and $0 \le x \le 2$, $\gamma < 1$), in which the N-coordinated P cations and C-coordinated R cations in an open framework bridged by cyanide groups (−C≡N−). Thus, the structures and electrochemical properties of PBA materials can be modulated via selecting various combinations of P and R transition metals together with several possible choices of the interstitial ions. The electrochemical energy storage in PBAs is usually based on the intercalation of ions (i.e., NH^{4+}, Na^+, K^+, Zn^{2+}, Mg^{2+}, Al^{3+}, etc.), along with corresponding redox reaction of transition metals. Common PBA materials include iron hexacyanoferrate (FeHCF), cobalt hexacyanoferrate (CoHCF), manganese hexacyanoferrate, nickel hexacyanoferrate (MnHCF), multi-metal hexacyanoferrate (i.e., CoNiHCF, MnFeHCF,

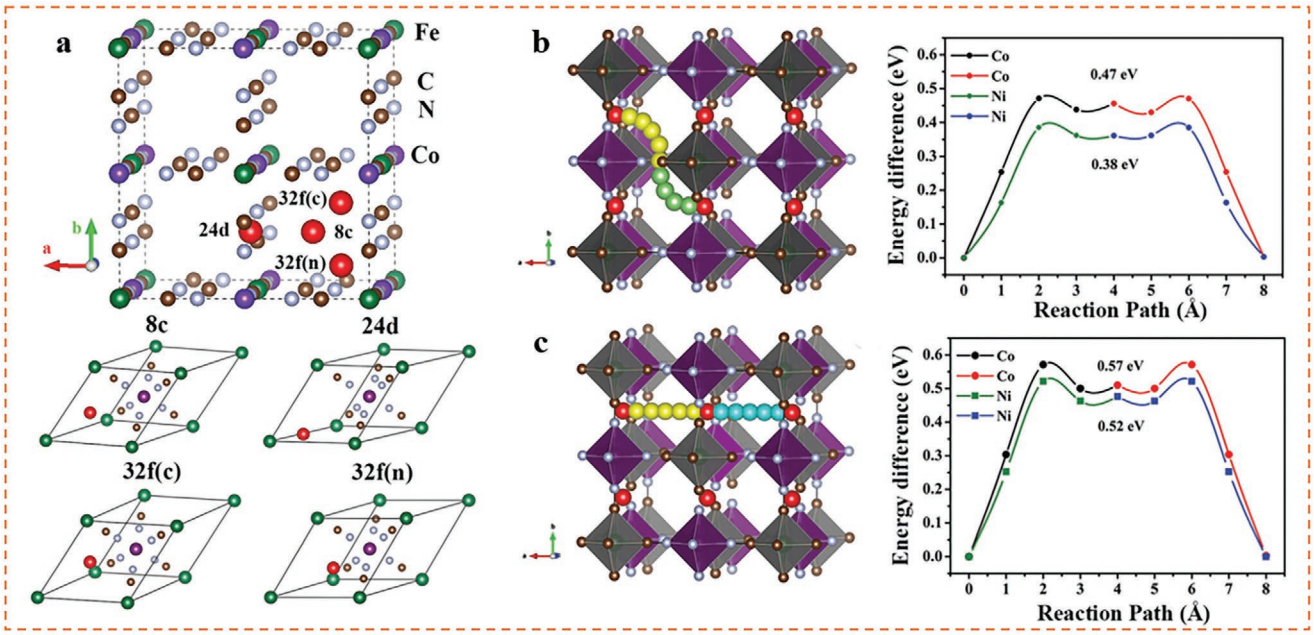

Figure 5. a) Crystal structure of NiCoHCF with the four possible interstices of 8c (body-centered), 24d (face-centered), 32f(n) (displaced from 8c sites toward N-coordinated corner), 32f(c) (displaced from 8c sites toward C-coordinated corner), b) non-linear and c) linear diffusion routes and corresponding migration energies. Reproduced with permission.[75] Copyright 2018, Wiley-VCH.

etc.), and other hexacyanoferrate compounds (Table S1, Supporting Information). For some PBAs like FeHCF, CoHCF, and MnHCF, both the P and R sites are redox active with different redox potentials, wherefore two plateaus are usually observed in their charge/discharge profiles, as well as higher capacities (100–175 mAh g^{-1}). However, some PBAs like NiHCF, ZnHCF, and CuHCF, only exhibit one redox-active site, since Ni, Zn, and Cu are electrochemically inert in the operating window of common electrolytes, and thereby, the capacity delivery of these compounds are usually <90 mAh g^{-1}.

4.1. FeHCF

FeHCF has two kinds of octahedrons, i.e., high-spin Fe^{HS} located in FeN_6 octahedrons and low-spin Fe^{LS} located in FeC_6 octahedrons, which are interconnected by −C≡N− bridges alternately to form a cubic open framework. Both the Fe^{HS} and Fe^{LS} participate in redox reactions, thus, the theoretical capacity of FeHCF is very high (≈170 mAh g^{-1}). However, since the Fe^{LS} is less active, the practical delivered capacity is much lower. For example, in aqueous batteries, the $Na_{1.52}Ni_{0.24}Fe_{0.76}$–$[Fe(CN)_6]_{0.95}$,[76] $K_2FeFe(CN)_6$,[77] and $K_2FeFe(CN)_6$[78] exhibit capacity of 106, 125, and 120 mAh g^{-1} for electrochemical storage of Na^+, Na^+/K^+, and K^+, respectively, which is far less than that of theoretical capacity. Furtherly, $FeFe(CN)_6$ also displayed capacity of 116 mAh g^{-1} in 5 M $Al(CF_3SO_3)_3$ electrolyte.[79] The limited utilization of Fe^{LS} result in insufficient lifespan, inferior rate capability, and low working voltage of FeHCF. Yang et al.[80] first reported that the high-voltage scanning can activate FeHCF as cathode in an $Zn(CF_3SO_3)_2$ water-in-salt electrolyte, $FeFe(CN)_6$ displayed an capacity of 75 mAh g^{-1} with capacity contribution of up to 60% from discharge voltage plateau at ≈1.5 V versus Zn/Zn^{2+}.

4.2. CoHCF

CoHCF has two plateaus corresponding to high-spin Co^{HS} and Fe^{LS}. CoHCF has been widely investigated as cathodes for Na^+-ion storage, for instance, hollow CoHCF,[81] CoHCF-Cit/CNT,[82] and $Na_2Ni_{0.4}Co_{0.6}$-$[Fe(CN)_6]$[70] presented capacities of 97.8, 107, and 85 mAh g^{-1} in Na^+-containing aqueous electrolytes, respectively. Ma et al.[74] developed and utilized $CoFe(CN)_6$ as cathode materials in an aqueous Zn-ion battery, in which both Co^{HS} and Fe^{LS} ions contributed to the two-electron energy storage process, and the aqueous rechargeable $Zn/CoFe(CN)_6$ cells displays a reversible capacity of 173.4 mAh g^{-1} at 0.3 A g^{-1} with discharge voltage plateau of 1.75 V versus Zn/Zn^{2+}. Besides, Peng et al.[75] reported that introducing inactive metal Ni could suppress capacity fading caused by excessive lattice distortion, thus, the high-quality $Na_{1.68}Ni_{0.14}Co_{0.86}[Fe(CN)_6]_{0.84}$ showed the best reversible Na^+-storage behavior with a specific capacity of ≈145 mAh g^{-1} and a remarkably improved cycle performance.

4.3. MnHCF

MnHCF displayed a high specific capacity and redox plateaus at high voltage among all simple PBAs, however, the crystal Jahn–Teller distortion effect restricted it long-term cycling. The volume changes between the charged and discharged MnHCF phases contributed to the capacity fading, which can be suppressed via reducing structural water content in the as-prepared material, metal substitution, as well as applying high-concentration electrolyte.[30] Song et al.[83] revealed that the removal of structural water benefited to the electrode performance of $Na_{2-\delta}MnHFC$ phase. Hu et al.[84] reported a concentration-gradient $Na_xNi_yMn_{1-y}Fe(CN)_6 \cdot nH_2O$ with high Ni content on the particle surface, the modified MnHCF delivered high reversible specific capacity of 110 mAh g^{-1} at 0.2 C, as well as outstanding cycling stability. Li et al.[85] developed $Na_{1.60}Mn_{0.833}Fe_{0.167}[Fe(CN)_6]$ with Na-rich cubic structure and dual-metal active redox couples to minimize the stress distortion during cycling, and exhibited capacity of 121 mAh g^{-1} at 0.1C in 1 M $NaClO_4$ in EC/DMC electrolyte, and an improved cycling performance. Furtherly, Jiang et al.[55] proposed Mn-rich $K_xFe_yMn_{1-y}[Fe(CN)_6]_w \cdot zH_2O$ as hosts for K+-ion storage in 22 M KCF_3SO_3 electrolyte, in which Fe substitution could mitigate the phase transitions upon discharge, and the high-concentration electrolyte could help decrease the dissolution of electrodes owing to the lack of free water. As a result, the cathode displayed capacity of 135 mAh g^{-1} at 0.5C, and superior cycling performance.

4.4. NiHCF

For NiHCF, there exists only one pair of voltage plateaus, attributing to the equilibrium voltage of the $[Fe(CN)_6]^{4-}/[Fe(CN)_6]^{3-}$ redox couple. Thus, it displays a reversible capacity of 65 mAh g^{-1} (in an organic Na^+-containing electrolyte) and a good rate performance.[68] During cycling, the lattice parameters of NiHCF negligibly change (<1%), which guarantee an unrivalled cycling stability, and are of great importance for application of long-life rechargeable batteries. Ren et al.[86] activated the Na^+ storage sites in NiHCF via controllable surface etching, which improved the discharge specific capacity up to 90 mAh g^{-1}, and displayed an outstanding rate capability of 71.0 mAh g^{-1} at 44.4 C. besides, when acting as host materials in multivalent ion batteries, the capacity delivery can be reduced due to the sluggish diffusion kinetics of multivalent ions. For instance, the $K_{1.51}Ni[Fe(CN)_6]_{0.954}$–$(H_2O)_{0.766}$[87] and $K_{0.02}Ni_{1.45}[Fe(CN)_6] \cdot 2.6H_2O$[88] displayed lower capacities of 48 and 46 mAh g^{-1} in 0.5 M $Mg(ClO_4)_2$ and 5 M $Al(CF_3SO_3)_3$ electrolytes, respectively.

4.5. Others

CuHCF, ZnHCF, and TiHCF have also been investigated as cathodes in batteries/super-capacitors. It is reported that the working potential of CuHCF is higher than that of NiHCF, while NiHCF presents much better cycling stability due to its poor crystallinity.[19] It is reported that $KCu[Fe(CN)_6]$[89] and $Na_2Cu_{0.6}Ni_{0.4}[Fe(CN)_6]$[73] displayed 60 and 62 mAh g^{-1} in aqueous $NaClO_4$ electrolytes, respectively. Besides, $Cu[Fe(CN)_6]_{Y0.37} \cdot 3.4H_2O$[90] has also been investigated as cathode material for proton batteries, with a

high specific capacity of 95 mAh g^{-1} at 1C, as well as a high rate capacity of 49 mAh g^{-1} at 4000C.

Wu et al.[91] reported the Zn^{2+}-insertion in $Zn_3[Fe(CN)_6]_2$ in 30 m $ZnCl_2$ "water-in-salt" electrolyte, which displayed a specific capacity of 95 mAh g^{-1} at 1C. Mai's group[92] revealed a selective K^+ insertion/extraction into/from CuHCF in a K^+-Zn^{2+} hybrid aqueous electrolyte, which displayed a high capacity of 79 mAh g^{-1} at 2C, and a superior rate capacity of 47 mAh g^{-1} at 300C.

Xie et al.[93] developed a new type of Prussian blue analog, $Na_{0.66}Ti[Fe(CN)_6]_{0.92}\cdot\square_{0.08}$, in which two kinds of Na^+ storage sites were provided by Fe^{LS} and Ti^{HS} ions, contributed to a high capacity of over 90 mAh g^{-1}, with two pairs of clear charge/discharge plateaus at 3.0 V/2.6 V and 3.4 V/3.2 V, respectively. This work broadened the categories of transition metals in PBA frameworks.

5. Optimization Strategies for High-Performance PBA Cathodes

One of the most important limitations in the previously reported PBA cathode materials is the low capacity delivery, which constrained the specific energy and power densities of the full batteries. Access to achieve the full theoretical capacity was mainly limited by the following obstacles: i) in some PBA materials, only the C-coordinated Fe is electrochemically active, i.e., only half of the available A-sites were utilized for the capacity delivery; ii) the occurrence of $[Fe(CN)_6]^{3-/4-}$ vacancies in PBA materials synthesized with a conventional co-precipitation method lowers the potential capacity that can be utilized; iii) water molecules bond to the N-coordinated transition metal ions around the $[Fe(CN)_6]^{3-/4-}$ vacancy not only decrease the specific capacity, but also deteriorate the cycling stability of electrodes. To address these issues, researchers have proposed a series of optimization strategies to enhance the energy storage properties of PBAs, i.e., reducing crystal vacancies and water content during synthesis, metal-substitution, designing novel morphology, constructing PBA-based composite materials, as well as applying high-concentration electrolytes. In this chapter, the above optimization strategies are summarized, which we hope can provide relevant guidance for the future development and design of more advanced PBA materials.

5.1. Reducing Crystal Vacancies and Crystal Water

In the early stages of the study, researchers usually prepared the PBA materials using the simple hydrothermal or chemical precipitation reactions with transition metal salts and $Fe[(CN)_6]^{4-}$ in aqueous electrolytes. These synthesis methods led to a lot of $[Fe(CN)_6]^{4-}$ vacancies in lattice structures, due to the imperfect crystal growth process, and these vacancies could be occupied by the coordination water, resulting in the decrease in ion/electron conductivities, as well as the occurrence of some side reactions. As a result, the obtained PBA electrodes could hardly reach their theoretical specific capacity, and the corresponding structural stability was severely deteriorated. Through tuning the synthesis method, an optimized crystal growth process could be achieved to obtain smaller content of crystal vacancies, and coordination waters,[94–96] and thus to enhance the capacity delivery of PBA electrodes.

Increasing the content of alkali metal ions in synthesis process and removing the interspace water by vacuum drying have been utilized to reduce the vacancies and coordinative water content in PBA materials. In 2015, Goodenough et al.[83] reported the removal of interspace water by vacuum drying to obtain a dehydrated $Na_2MnFe(CN)_6$. The crystal structures of the hydrated/dehydrated $Na_{2-\delta}MnHCF$ were detected and simulated by a combined analyses XRD and time-of-flight (TOF) neutron diffraction. Upon vacuum drying, the monoclinic hydrated $Na_{2-\delta}MnHCF$ (space group of $P21/n$, a = 10.5864 Å, b = 7.5325 Å, c = 7.3406 Å, and β = 92.119°) transformed to a rhombohedral dehydrated $Na_{2-\delta}MnHCF$ (space group = $R\bar{3}$, $a = b$ = 6.5800, c = 18.9293 Å), as shown in **Figure 6**a,c. The interstitial H_2O played a critical role on the electrochemical voltage profile of electrodes. When operated in 1 M $NaClO_4$ in 1:1 diethyl carbonate/ethylene carbonate electrolyte, Mn^{3+}/Mn^{2+}-N and Fe^{3+}/Fe^{2+}-C redox reactions accounted for the two voltage plateaus in the hydrated $Na_{2-\delta}MnHCF$ electrode (Figure 6b), while they overlapped to form only one plat voltage plateau at ≈3.5 V (Figure 6d). The change of discharge platform for the dehydrated sample was mainly due to the removal of interstitial H_2O, which induced a larger rotation of the (C≡N)− anion from the Mn−N≡C−Fe bond axis, shorted the Mn···Fe distance, lowered the volume of cell unit, as well as reduced the energy separation of Mn^{3+}/Mn^{2+}-N and Fe^{3+}/Fe^{2+}-C redox couples. Consequently, the dehydrated $Na_{2-\delta}MnHCF$ presented a flat charge and discharge platform with a reversible capacity of 150 mAh g^{-1} at 3.5 V in a sodium half-cell, and 140 mAh g^{-1} with a hard-carbon anode.

Wu et al.[97] reported that increasing NaI concentration in synthesis electrolyte could benefit to generate the low-defect $Na_{1.33}Fe[Fe(CN)_6]_{0.82}$ nanoparticles, as a competent cathode material for Na^+ storage. Benefiting from the suppressed lattice defects and well defined nanocubic morphology, the $FeFe(CN)_6$ electrode showed a greatly enhanced capacity (125 mAh g^{-1}), a robust rate capability (102 mAh g^{-1} at rate of 20C), and an excellent cycling stability (capacity retention of 83% over 500 cycles). Dou's group[98] reported a Na-rich $Na_{1+x}Fe[Fe(CN)_6]$ as superior cathode material for sodium-ion batteries. The Na-rich $Na_{1+x}Fe[Fe(CN)_6]$ was synthesized using $Na_4Fe(CN)_6$ as precursor in solutions with different NaCl concentrations (PB-1, 0 M; PB-3, 1.2 M; PB-5, 6.16 M), and their XRD Rietveld refinement results (Figure 6e) indicated a clearly increased entrance of Na^+ ions into the crystal lattice of $Na_{1+x}Fe[Fe(CN)_6]$ framework, leading to an obvious increase of the lattice parameter a from 10.3028 Å (PB-1) to 10.3304 Å (PB-5). With more Na^+-ion occupation in the PB framework, the amount of C≡N groups increased, and the amount of O atoms, which come from the coordinated water, decreased gradually from the PB-1 to the PB-5, suggesting a decreased content of $[Fe(CN)_6]^{4-}$ vacancies and crystal water. Consequently, PB-5 electrode displayed a capacity of 103 mAh g^{-1} at the current density of 20 mA g^{-1}, which is larger than that of the PB-1 (89.5 mAh g^{-1}). PB-5 electrode also showed excellent cycling stability (97% of capacity retention after 400 cycles) (Figure 6f).

Slowing down the crystallization rate has also been regarded as an effective way to reduce crystal defects. For a rapid

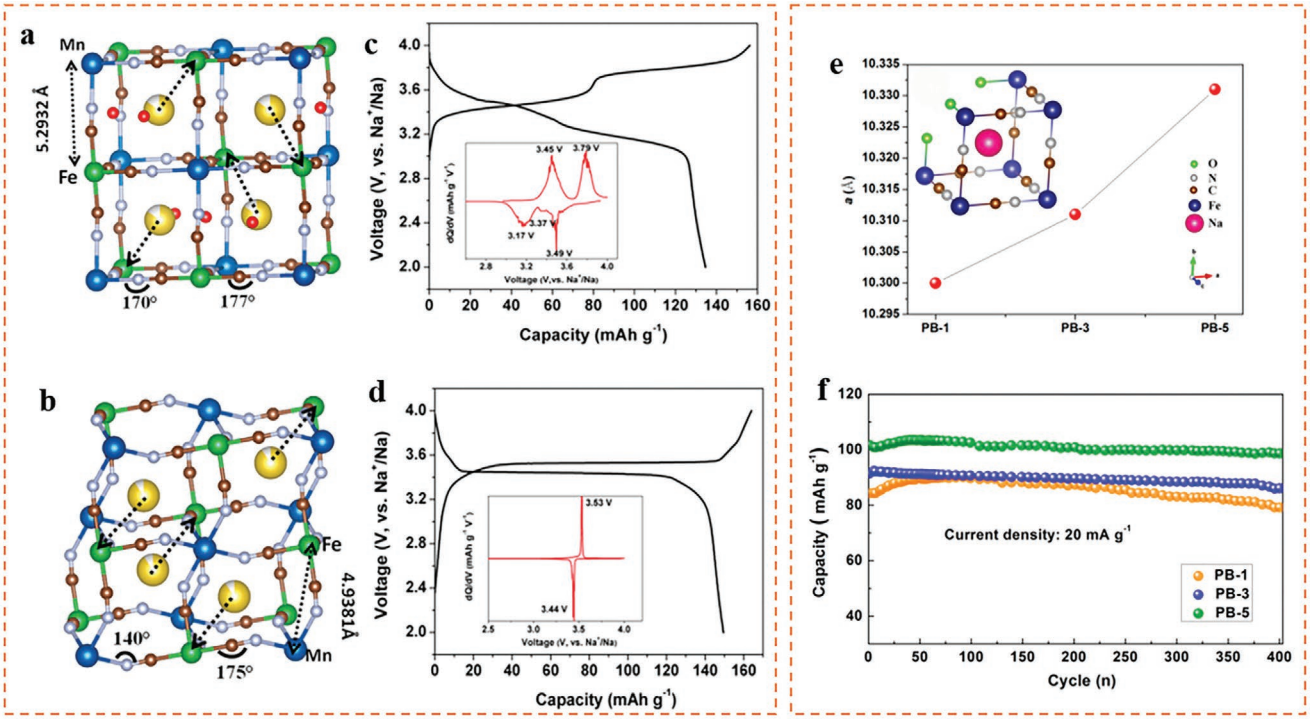

Figure 6. Reducing crystal water and increasing alkaline cation contents to advance the electrode performance. a) crystal structure of hydrated $Na_{2-\delta}MnHCF$ and c) corresponding electrochemical profile; b) crystal structure of dehydrated $Na_{2-\delta}MnHCF$ and d) corresponding electrochemical profile; Reproduced with permission.[83] Copyright 2015, American Chemical Society; e) Lattice parameters changes of the $Na_{1+x}Fe[Fe(CN)_6]$ powders and the crystal structure of the $Na_{1+x}Fe[Fe(CN)_6]$ framework, f) Cycling performance of $Na_{1+x}Fe[Fe(CN)_6]$ electrodes. Reproduced with permission.[98] Copyright 2015, American Chemical Society.

nucleation and growth process, the control of PBA particle size during synthesis process is difficult in aqueous solution. In 2015, Liu et al.[99] prepared $Na_{1.7}FeFe(CN)_6$ as host for Na^+ ion storage. With the sodium citrate as a chelating agent during synthesis, the crystallization rate slowed down successfully, and consequently improved the crystallinity of $Na_{1.7}FeFe(CN)_6$ (**Figure 7**a,b). High-crystallinity was directly related to the lower water content and higher sodium content in the crystal. Furtherly, with higher crystallinity, the $Na_{1.7}FeFe(CN)_6$ showed highly reversible electrochemical reactions, with a high capacity delivery (120.7 mAh g^{-1} @ 200 mA g^{-1}), and a high rate performance (73.6 mAh g^{-1} @ 1200 mA g^{-1}), as well as enhanced cycling performance in 1 M $NaClO_4$ in PC/EC (v/v = 1:1) electrolyte (Figure 7c,d). Lower crystallization rate can also be achieved via changing the solvent from water to ethylene glycol, as well as using a low-temperature solvothermal method. In 2017, Wang's group[78] prepared uniform $K_2Fe[Fe(CN)_6]$ dehydrate nanocubes with an edge length of ≈200 nm using ethylene glycol based electrolyte. The obtained $K_2Fe[Fe(CN)_6]$ nanocubes presented much smaller particle size than that synthesized in aqueous electrolyte (Figure 7e,f). When applied as host material for K^+ ion storage, the $K_2Fe[Fe(CN)_6]$ electrode showed a high discharge capacity of 120 mAh g^{-1} (at current density of 200 mA g^{-1}), and an excellent cycling stability with >85% capacity retention over 500 cycles at current of 21.4 C in 0.5 M K_2SO_4 electrolyte (Figure 7g,h). In summary, the above methods, including annealing treatment, increasing salt concentration and applying chelating agent during synthesis, etc., is effective to synthesize the PBA materials with lower crystal vacancies and crystal waters. With reduced crystal defects, optimized electrochemical performance can be achieved, due to the reduced side reactions, enhanced electronic/ionic conductivities, as well as the optimized redox reactions.

5.2. Metal-Substitution

Metal substitution control is a general method to tune the electrochemical performance of electrodes.[100] For the most widely used PBA materials ($A_xM[Fe(CN)_6]_y \cdot nH_2O$), there exist two type of transition metal ions in the lattice framework. When M is a transition metal such as Ni, Cu, Zn, N-coordinated M is electrochemically inert, and only C-coordinated Fe^{2+} can undergo redox conversion. Owing to the single active redox site (one-electron transfer Fe^{2+}/Fe^{3+}), this type of PBAs shows a low theoretical specific capacity (<70 mAh g^{-1}), excellent electrical conductivity, as well as good cycle stability and rate performance. However, when M is Fe, Co, Mn, etc., there exists two types of redox reaction sites (two-electron transfer), i.e., Fe^{2+}/Fe^{3+} and M^{2+}/M^{3+}, leading to higher capacity delivery (≈170 mAh g^{-1}), but with poor cycle stability. For example, Wessells et al.[28,27] reported that $K_{0.6}Ni_{1.2}Fe(CN)_6 \cdot 3.6H_2O$ and $K_{0.71}Cu[Fe(CN)_6]_{0.72} \cdot 3.7H_2O$ electrodes showed a long lifespan (5000–40 000 cycles) as hosts for Na^+ and K^+ storage, but they exhibited a low capacity below 70 mAh g^{-1}, while Su et al.[78] reported that the $K_2FeFe(CN)_6 \cdot 2H_2O$ offered a higher capacity of 120 mAh g^{-1}, but with a low lifespan of about 500 cycles. To achieve both higher cycling stability and capacity delivery

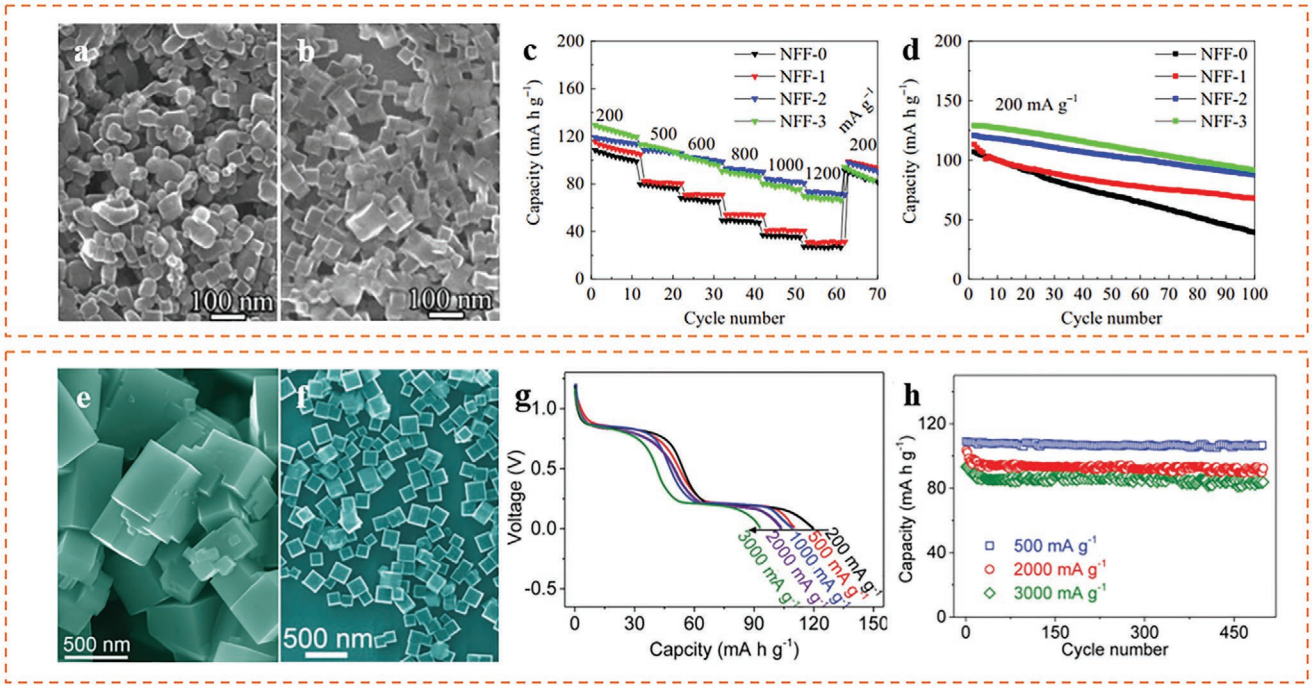

Figure 7. Slowing down the crystallization rate during synthesis to achieve higher electrode performance. As prepared $Na_{1.7}FeFe(CN)_6$ particles a) without and b) with sodium citrate; comparison of c) rate performance and d) cycling performance of electrodes. Reproduced with permission.[99] Copyright 2015, Elsevier; The $K_2Fe[Fe(CN)_6]$ particles synthesized in e) H_2O and f) ethylene glycol based electrolytes; g) rate performance and h) cycling performance of $K_2Fe[Fe(CN)_6]$ electrodes. Reproduced with permission.[98] Copyright 2016, Wiley-VCH.

of $K_xM[Fe(CN)_6]_y \cdot nH_2O$ electrode, Hu et al.[55] developed an Fe-substituted Mn-rich $K_xFe_yMn_{1-y}[Fe(CN)_6]_w \cdot zH_2O$ cathode for aqueous K^+-ion batteries in 22 M KCF_3SO_3 (water in salt) electrolyte. The $K_{1.98}Mn[Fe(CN)_6]_{0.94} \cdot 0.57H_2O$ (KMnHCF) and $K_{1.85}Mn_{0.33}Fe_{0.67}[Fe(CN)_6]_{0.98} \cdot 0.77H_2O$ (KFeMnHCF-3565) were prepared to reveal the role of Fe-substitution. Comparing with KMnHCF electrode (capacity/voltage decay in 40 cycles, **Figure 8**a), the KFeMnHCF-3565 electrode exhibited nearly no capacity and/or voltage decay within the initial 40 cycles at 10C (Figure 8b). Comparing with KMnHCF electrode, not only the formation of trigonal phase at the end of the charging process was reduced (showing highly reversible phase transformation during cycle), but also the electronic and K^+-ion conductivities was enhanced for KFeMnHCF-3565 electrode, as confirmed by DFT calculation results (smaller bad gap and diffusion activation energy after Fe substitution, Figure 8c,d). As a result, the KFeMnHCF-3565 electrode presented impressive performance of high capacity (135 mAh g^{-1} at 0.5 C and 94 mAh g^{-1} at 100 C), with a capacity retention of 90% over 10 000 cycles (Figure 8e).

Wang et al.[76] investigated the effect of low-level Ni substitution on the electrochemical performance of Na-rich $Na_xFeFe(CN)_6$ (NaFeHCF) cathode. The NaFeHCF was synthesized by a citrate-assisted controlled crystallization co-precipitation method. The Ni substitution in NaFeHCF (without any change in the basic crystal structure) could not only stabilize the crystal structure, but also enhance the intrinsic electric conductivity. Consequently, the $NaNi_{0.23}Fe_{0.77}HCF$ delivered high discharge capacity of 105.9 mAh g^{-1} at 200 mA g^{-1} and 73.1% capacity retention over 1000 cycles at 1000 mA g^{-1}. Peng et al.[75] furtherly investigated the electrochemical performance of a series of $Ni_xCo_{1-x}[Fe(CN)_6]$ PBA materials with different Ni/Co ratios. The electrochemical performances of $Na_{0.79}Ni[Fe(CN)_6]_{0.74}$ (LQ-NiFe), $Na_{0.86}Co[Fe(CN)_6]_{0.73}$ (LQ-CoFe), $Na_{0.71}Ni_{0.25}Co_{0.75}[Fe(CN)_6]_{0.75}$ (LQ-NiCoFe), and $Na_{1.68}$ $Ni_{0.14}Co_{0.86}[Fe(CN)_6]_{0.84}$ (HQ-NiCoFe) cathodes were compared (**Figure 9**a,b). Among all the electrodes, two pairs of well-defined and symmetric oxidation/redox peaks at 3.42/3.22 and 3.86/3.73 V were observed for HQ-NiCoFe electrode, correlating to two reversible Na^+ insertion/extraction into/out of the structural framework (representing C-coordinated Fe^{2+}/Fe^{3+} and N-coordinated Co^{2+}/Co^{3+} redox reactions), while the oxidation/redox peaks of Co^{2+}/Co^{3+} of LQ-NiCoFe and LQ-CoFe are inconspicuous with large polarizations (showing low platform capacity). Thus, HQ-NiCoFe displayed the best rate performance. Reversible phase transition mechanism (between cubic and monoclinic) was revealed for HQ-NiCoFe electrode upon Na^+-ion extraction process (Figure 9c). The authors attributed the high reversibility of Na^+ insertion/extraction in HQ-NiCoFe to the following two reasons: i) the excellent structural stability of HQ-NiCoFe framework is mainly due to the small lattice variation (less than 3%) during cycle via introducing 0.14 Ni in per formula unit, ii) the fewer of the $Fe(CN)_6$ vacancies and water molecules prevented the collapse and deterioration of HQ-NiCoFe framework during cycle. Consequently, HQ-NiCoFe exhibited a high specific capacity of 145 mAh g^{-1} (1.68 electron transfer), and an impressive cycling stability (90% of capacity retention over 600 cycles at current of 5C, CE of 100%).

Li et al.[85] also reported the Fe substitution in $Na_{1.60}Mn_{0.833}Fe_{0.167}[Fe(CN)_6]$ (NaMnFe-HCF) to minimize the stress distortion by restraining Mn^{2+} dissolution and the trigonal-cubic phase transition (common issues in Mn-based PBAs). The pure Mn-based hexacyanoferrate (NaMn-HCF) showed the

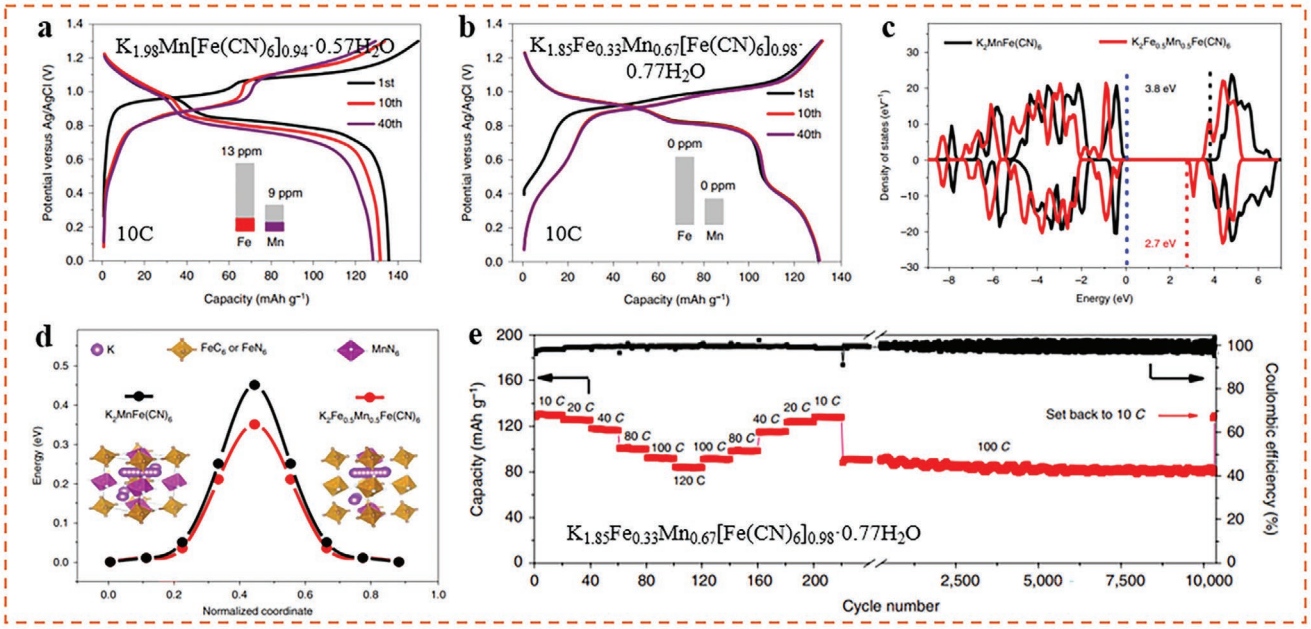

Figure 8. Fe-substituted Mn-rich $K_xFe_yMn_{1-y}[Fe(CN)_6]_w\cdot zH_2O$ cathode for enhanced cycling performance. Charge/discharge profiles of the a) KMnHCF and b) KFeMnHCF electrodes; c) Density of states for the KMnHCF and KFeMnHCF model structures; d) Migration energy barriers of the K+-ion diffusion within the lattice of the KMnHCF and KFeMnHCF model structures; f) Rate capability and long-term cycling performance of the KFeMnHCF-3565 electrode. Reproduced with permission.[55] Copyright 2019, Springer Nature.

trigonal structure with $a = b = 7.539$ Å, $c = 17.9193(1)$ Å in space group *R*-3 (**Figure 10**a), while the NaMnFe-HCF presented a face-centered-cubic (FCC) structure with the lattice parameters $a = b = c = 10.515(1)$ Å in space group *Fm*-3*m* (Figure 10b). The different crystal structures of NaMn-HCF and NaMnFe-HCF are determined by the different locations of Na^+ ions in

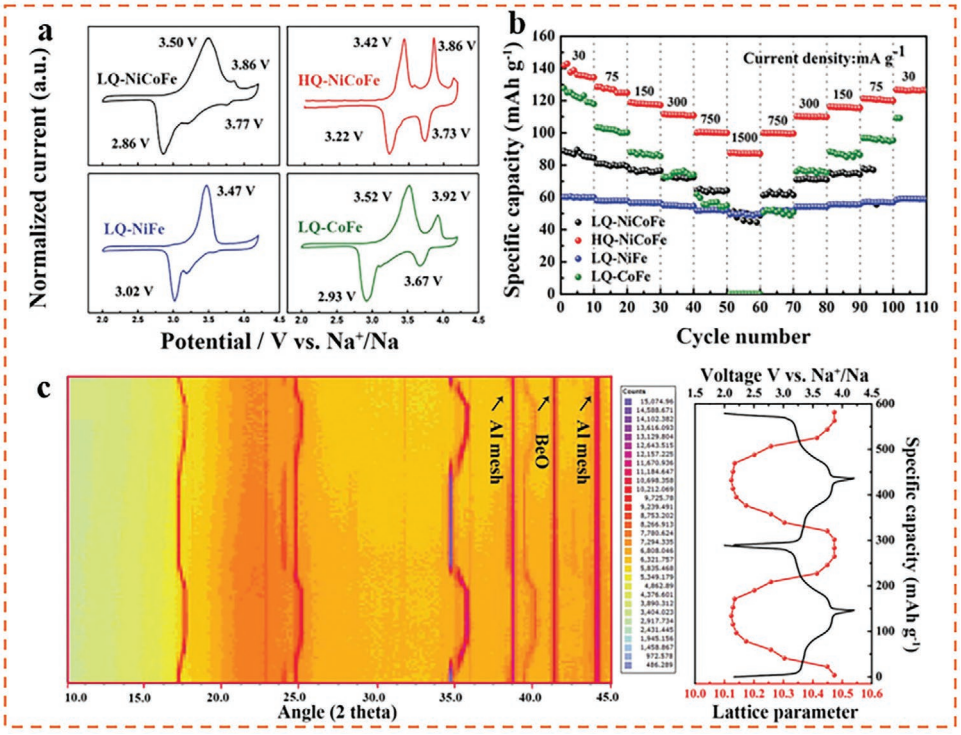

Figure 9. The comparison of a) CV curves and b) rate performances of $Na_{0.79}Ni[Fe(CN)_6]_{0.74}$ (LQ-NiFe), $Na_{0.86}Co[Fe(CN)_6]_{0.73}$ (LQ-CoFe), $Na_{0.71}Ni_{0.25}Co_{0.75}[Fe(CN)_6]_{0.75}$ (LQ-NiCoFe), and $Na_{1.68}Ni_{0.14}Co_{0.86}[Fe(CN)_6]_{0.84}$ (HQ-NiCoFe) cathodes; c) In situ XRD patterns of HQ-NiCoFe under cycling at a current density of 15 mA g^{-1}. Reproduced with permission.[75] Copyright 2018, Wiley-VCH.

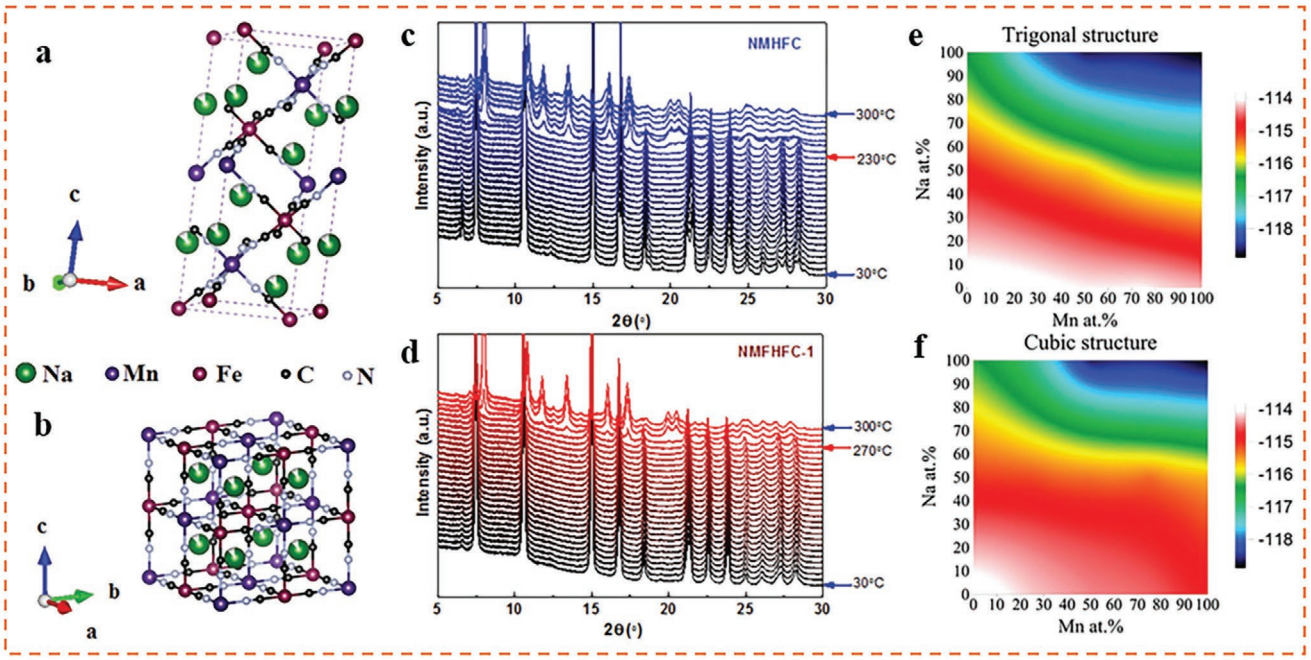

Figure 10. Crystal structures of a) NMHFC and b) NMFHFC; structural evolution of c) NMHFC and d) NMFHFC during heating from 30 to 300 °C; 3D surface plot of total energy difference as a function of the Na ion occupancy percentage and the Mn atomic occupancy (Mn/Fe ratio) in the framework of e) cubic and f) trigonal structures, respectively. Reproduced with permission.[85] Copyright 2019, Wiley-VCH.

the unit structures, i.e., Na^+ ions in NaMn-HCF occupied the 6c positions in the voids of the structure, and deviated toward Mn atoms of NaMn-HCF, while Na^+ ions occupied 8c positions in the middle of the voids in NaMnFe-HCF. The result demonstrated that the trigonal structure of NaMn-HCF can be tuned to the cubic phase after the introduction of the second electrochemically active Fe. This Fe-substitution induced structure variation improved the thermal stability of Mn-based hexacyanoferrate, i.e., the phase decomposition of NaMnFe-HCF (started from 270 °C) was higher than that of the NaMn-HCF (started from 230 °C), as shown in Figure 10c,d. High thermal stability of electrode materials are intimately related to the corresponding cycling stability.[101,102] The authors also revealed that both structures become more stable with higher Na and Mn contents, and the cubic NaMnFe-HCF presented lower energy variation (during cycle) than that of NaMn-HCF, as well as the lower volume change, which was responsible for higher electrode cycle stability (Figure 10e,f). As a result, the NaMnFe-HCF electrode delivers high energy density (436 Wh kg^{-1}) and excellent cycle life (80.2% capacity retention over 300 cycles) as host for Na^+ storage. In summary, the enhancing effect of metal substitution in PBA materials is mainly attributed to a combination of optimized crystal structure, enhanced thermal stability, improved electronic/ionic conductivity, as well as the minimized lattice variation during cycle.

5.3. Constructing Concentration Gradient and Core–Shell Structure

In addition to the direct metal doping, the crystal structure of PBA materials can be further stabilized via constructing concentration gradient and/or core–shell structure. For instance, Hu et al.[84] reported a $Na_xNi_yMn_{1-y}Fe(CN)_6 \cdot nH_2O$ (g-NiMnHCF) material with a concentration gradient of Ni content increased gradually from the inside of the particle to the surface. Concentration-gradient particles were prepared via a facile and scalable co-precipitation process (**Figure 11**a), in which the Ni^{2+} solution was slowly pumped into the Mn^{2+} solution to obtain a mixture with increasing Ni^{2+} concentration, and the resultant mixture of Ni^{2+}/Mn^{2+} was precisely pumped into a $Na_4Fe(CN)_6$ solution to form a precipitate under constant magnetic stirring. The obtained structure of g-NiMnHCF was special and strong enough to reduce the stress and cumulative damage during cycling, thus prevented the fractures observed in homogeneous NiMnHCF samples (Figure 11b–g), and thus improved the cycling performance. As a result, the g-NiMnHCF cathode displayed an improved electrochemical performance (high reversible specific capacity of 110 mAh g^{-1} at 0.2 C, outstanding cycling stability with 93% retention after 1000 cycles at 5 C) comparing the homogeneous NiMnHCF cathode.

Yin et al.[103] investigated the electrochemical performance of a highly crystallized core–shell Co/Ni hexacyanoferrate coated by Ni-HCF (CoNi-HCF@Ni-HCF), which was fabricated by using an in situ self-assembly method (**Figure 12**a). TEM figures identified that the Ni-HCF was uniformly coated on the surface of CoNi-HCF and forms a smooth shell with a thickness of 15 nm (Figure 12b). This specially designed structure suppresses lattice distortion and avoids side reactions during the Na^+ insertion and extraction process. Through comparing the CV curves of CoNi-HCF and CoNi-HCF@Ni-HCF electrodes, the authors revealed that the oxidation peaks at 4.15 V was almost disappeared for CoNiHCF@Ni-HCF electrode, demonstrating the suppressed side reaction in the electrode/electrolyte

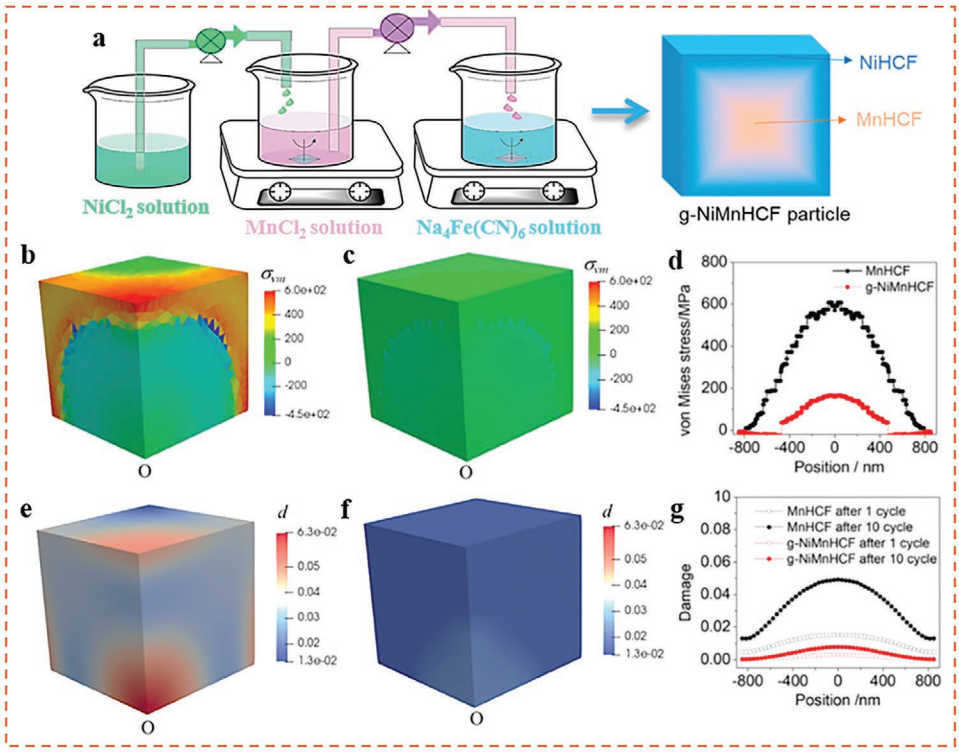

Figure 11. a) Schematics illustration of the preparation progress of the g-NiMnHCF; modulated von Mises stress (σ_{vm}) distribution in b) MnHCF and c) g-NiMnHCF during cycling; and d) comparison of modulated von Mises stress profiles of MnHCF and g-NiMnHCF; damage distribution of e) MnHCF and f) g-NiMnHCF materials after 10 cycles, respectively. g) Comparison of damage profiles of MnHCF and g-NiMnHCF after 10 cycles. Reproduced with permission.[84] Copyright 2020, American Chemical Society.

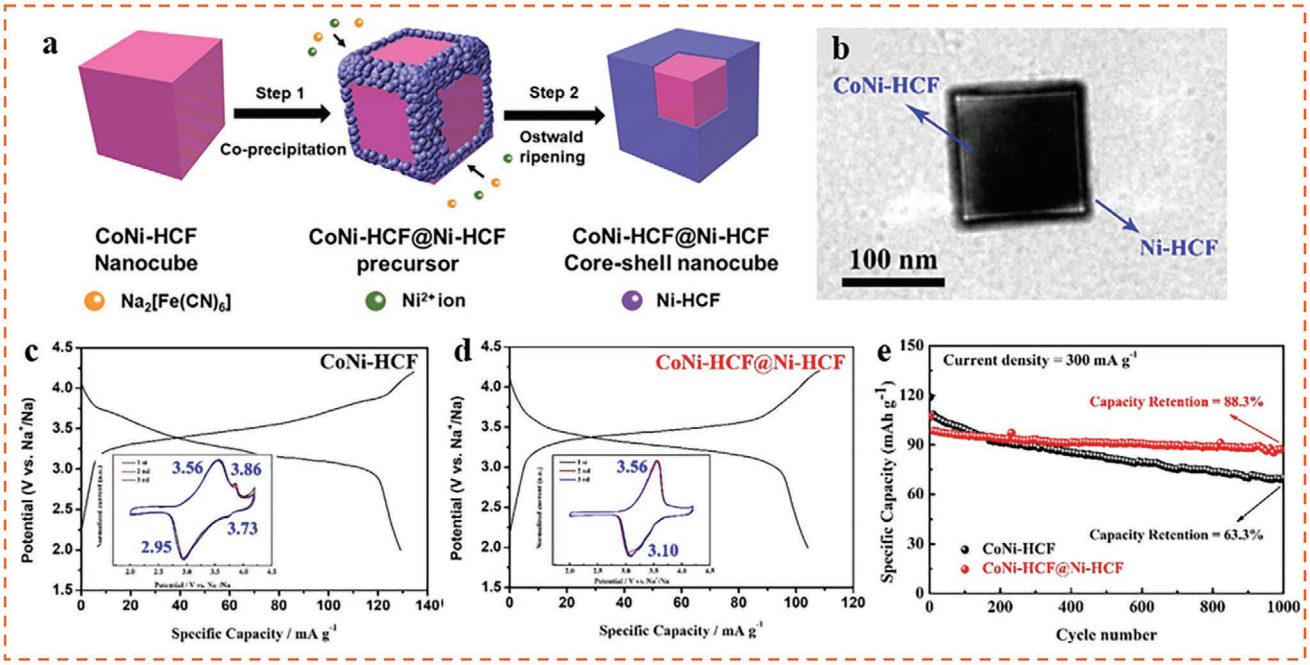

Figure 12. a) Synthesis procedure and b) TEM morphology of CoNi-HCF@Ni-HCF core–shell nanocubes; charge/discharge voltage profiles of c) CoNi-HCF and d) CoNi-HCF@Ni-HCF; e) long-term cycling performance of 300 mA g^{-1}. Reproduced with permission.[103] Copyright 2019, Wiley-VCH.

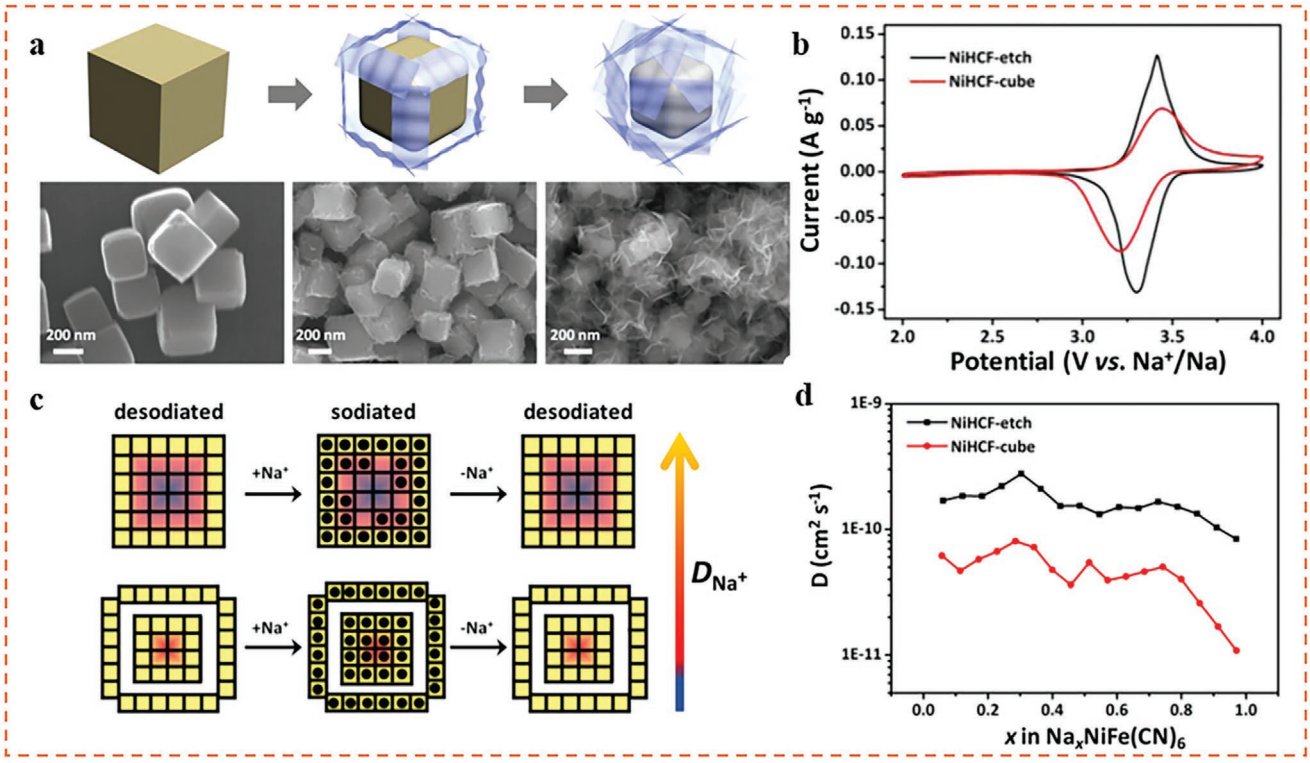

Figure 13. a) Schematic diagrams and SEM images of the NiHCF products after different etching time; b) comparison of CV curves of NiHCF-cube and NiHCF-etch; c) Outside-in diffusion route of Na^+ in NiHCF-cube and NiHCF-etch; d) The calculated diffusion coefficients versus state of discharge. Reproduced with permission.[86] Copyright 2017, American Chemical Society.

interface at voltages higher than 4.0 V (Figure 12c,d). Although the reversible capacity delivery reduced slightly from 129.2 to 104.3 mAh g^{-1} after coating, the CoNi-HCF@Ni-HCF electrode shows better rate and cycle performance (Figure 12e). In summary, constructing concentration gradient and core–shell structures, the side reactions in electrode/electrolyte interface and the stress and cumulative damage during cycling can be effectively suppressed, as well as the enhanced electrochemical electrode performance.

5.4. Novel Morphology Design for Faster Ion Transport

In recent years, researchers also explored the morphology/property relationship between the active materials morphology and corresponding electrochemical properties.[104] For PBA materials, the insufficient utilization of Fe^{2+}/Fe^{3+} redox couple was an obstacle for practical usage. To activate the Na^+ ion storage in $Ni[Fe(CN)_6]$, Ren et al.[86] reported a unique NiHCF nanoflower cathode using a surface etching approach (NiHCF-etch), which included a co-precipitation synthesis of NiHCF cube, and subsequent alkaline corrosion process (**Figure 13**a). After etching, the BET surface area increased from 12.7 to 38.0 m^2 g^{-1}, showing higher electrode/electrolyte interface for ion/charge transfer. NiHCF-etch electrode presented a much sharper redox peak comparing with that of the pristine NiHCF-cube, indicating that the NiHCF-etch electrode presented higher specific capacity as well as faster kinetics for Na^+ insertion/extraction kinetics (Figure 13b). Figure 13c showed the solid-state diffusion process of Na^+ in electrodes, comparing with the NiHCF-cube electrode that NiHCF-etch electrode presented a much shorter distance for Na^+ ions diffusion to occupy all of the insertion sites, and larger proportion of the reaction sites in central area could be accessed. GITT was employed to analyze the solid-state diffusion kinetics of Na^+, the calculated D_{GITT} for the NiHCF-cube and NiHCF-etch were between 10^{-10}–10^{-11} and 10^{-9}–10^{-10} cm^2 s^{-1}, respectively (Figure 13d). Due to the enhanced diffusion kinetics, the NiHCF-etch electrode exhibits an extremely high specific capacity of 90 mAh g^{-1}, high rate capability of 71.0 mAh g^{-1} at 44.4 C, as well as excellent cycle life over 5000 times.

Hollow particles are an important class of materials with large internal cavities and thin shells, which present wide applications in energy storage fields. Hollow PBA materials can be obtained via a facile synthesis process.[105] Wei's group[81] reported a universal MOF template strategy for fabricating hollow polyhedrons of cobalt hexacyanoferrate (CoHCF) as host material for Na^+ storage in aqueous electrolyte. ZIF-67 is one of MOF materials assembled by linking the Co^{2+} and imidazolate, and Co^{2+} ions in the framework can easily disassociate in an aqueous solution and released Co^{2+} into electrolyte. These Co^{2+} ions can further coordinate with $[Fe(CN)_6]^{4-}$ ions to form solid Co-HCF precipitates on the ZIF-67 surface. With gradual consumption of the ZIF-67 cores, the Co-HCF hollow structures gradually formed (**Figure 14**a). Finally, Co-HCF hollow structure was obtained with rough external surfaces composing of numerous nanoparticles with shell thickness of 150 nm. The obtained hollow dodecahedrons possessed an ultra-high BET

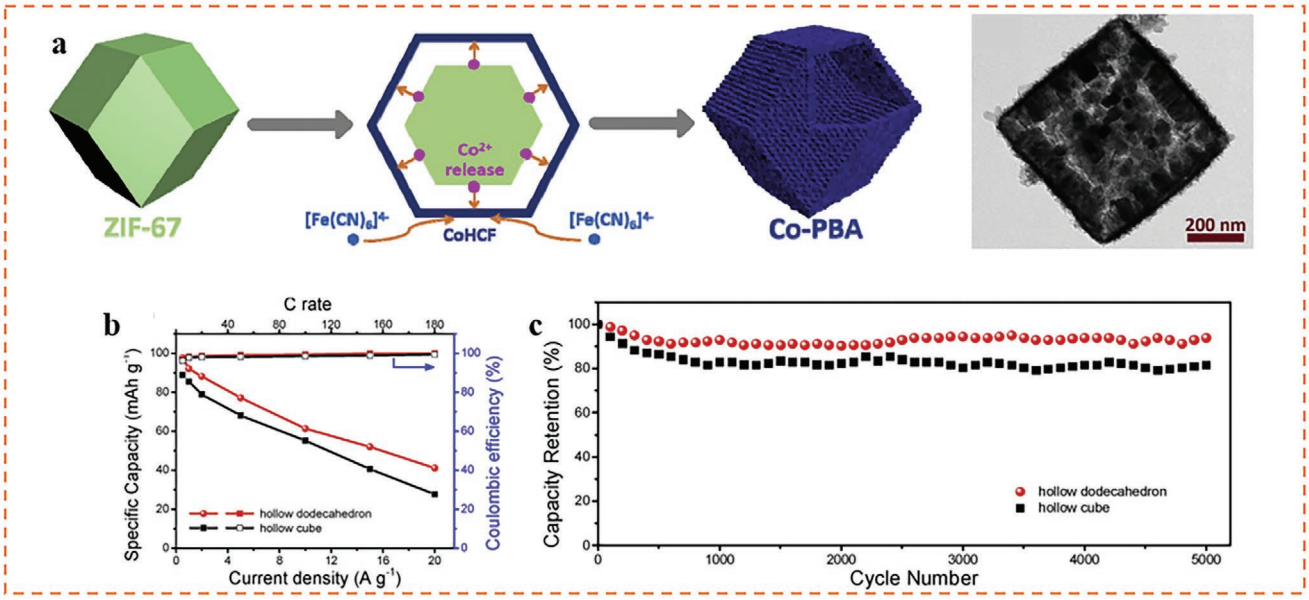

Figure 14. a) Schematic illustration of the formation mechanism of CoHCF hollow cubes; comparison of b) rate and c) cycling performance of CoHCF-cube and CoHCF hollow cubes. Reproduced with permission.[81] Copyright 2019, Elsevier.

specific surface area of 167 m g^{-1}, which was of great benefit for rapid ion/charge transportation. Comparing with the normal Co-HCF cube, the hollow Co-HCF exhibited much higher rate and cycling performance (Figure 14b,c). Furtherly, authors also presented the excellent hybrid Na-ion cells (carbon anode, hollow CoHCF cathode) with high specific power of 30 kW kg^{-1}, and superior cycling performance of over 3000 cycles. In summary, with simple etching approach and template strategy, we can synthesize PBA materials with novel morphologies, which provide higher electrode/electrolyte interface area for charge/ion transfer, consequently, the enhanced diffusion kinetics of electrode (high power density) can be achieved, as well as the superior cycling performance.

5.5. PBA-Based Composite Materials

The utilization of composite material, which is composed with active materials and other materials (e.g., carbon based materials) via physical or chemical binding, brings unexpected electrode performances. In 2015, Yang et al.[106] reported a reduced graphene oxide–PB composite as cathode for sodium-ion batteries. The product was obtained via heat-treating the graphene oxide–PB composite (GOPC), which could release the coordinated water from PB framework through electron exchange between the cubic PB particles and graphene oxide (GO) (**Figure 15**a). After heat-treatment, the PB was clearly well covered by RGO, and the resulted secondary particles reached ≈7–10 µm, which is an ideal particle size for industrial application (Figure 15b,c). This kind of composite material improved the conductivity (e.g., electrode depolarization effect[107]), removed the coordination water in the PB, reduced the occurrence of side reactions, thus, the obtained RGOPC3 electrode presented high rate performance and excellent cycling stability (163.3 mAh g^{-1} at 30 mA g^{-1}, capacity retention of 91.9% over 500 cycles at 200 mAh g^{-1}), as shown in Figure 15d,e.

Surface coating has been regarded as one of the effective methods to enhance electrode performance.[108,109] Tang et al.[110] reported a Fe-HCF microcubes encapsulated by conductive polypyrrole (PPy) to form Fe-HCF@PPy composites. With PPy coating, the obtained Fe-HCF@PPy exhibited a rougher surface comparing with the pure Fe-HCF (**Figure 16**a,d). The electrochemical process of the electrodes was tested by CV curves (Figure 16b,e). The side reactions (oxidation peak beyond 4.10 V in CV curves) of Fe-HCF disappear after PPy coating, indicating that PPy coating can restrain the side reactions between Fe-HCF and electrolyte. Comparing with Fe-HCF, the CV peaks of Fe-HCF@PPy-2 overlapped very well during scanning, indicating a more reversible redox reaction. Besides, the potential difference between the cathodic and anodic peaks for Fe-HCF@PPy-2 sample is smaller than that of Fe-HCF (220 mV vs 430 mV), indicating the reduced polarization due to the enhanced conductivity after PPy coating. SEM results also indicated the well preserved cubic morphology of Fe-HCF@PPy, while the Fe-HCF was partially destroyed, demonstrating the enhanced structure stability (Figure 16c,f). Thus, PPy coating acted as an electronic conductor to enhance electrical conductivity and a protective layer to inhibit side reactions, making the material have excellent rate performance and cycle stability (75 mAh g^{-1} at 3000 mA g^{-1}, and capacity retention of 79% after 500 cycles at 200 mA g^{-1}).

Introducing capacitive contribution can greatly enhance the electrode capacity delivery.[111] Lu et al.[112] reported (in 2017) the ZnHCF@MnO_2 composite as cathode for aqueous Zn ion batteries. In aqueous electrolyte, Zn^{2+} ions can adsorb on surface of 2D MnO_2 nanosheets due to the electrostatic interaction, then the subsequent dropwise addition of $K_3Fe(CN)_6$ during the aging process resulted in the formation of the ZnHCF@MnO_2 composite (**Figure 17**a). TEM morphology of ZnHCF@MnO_2

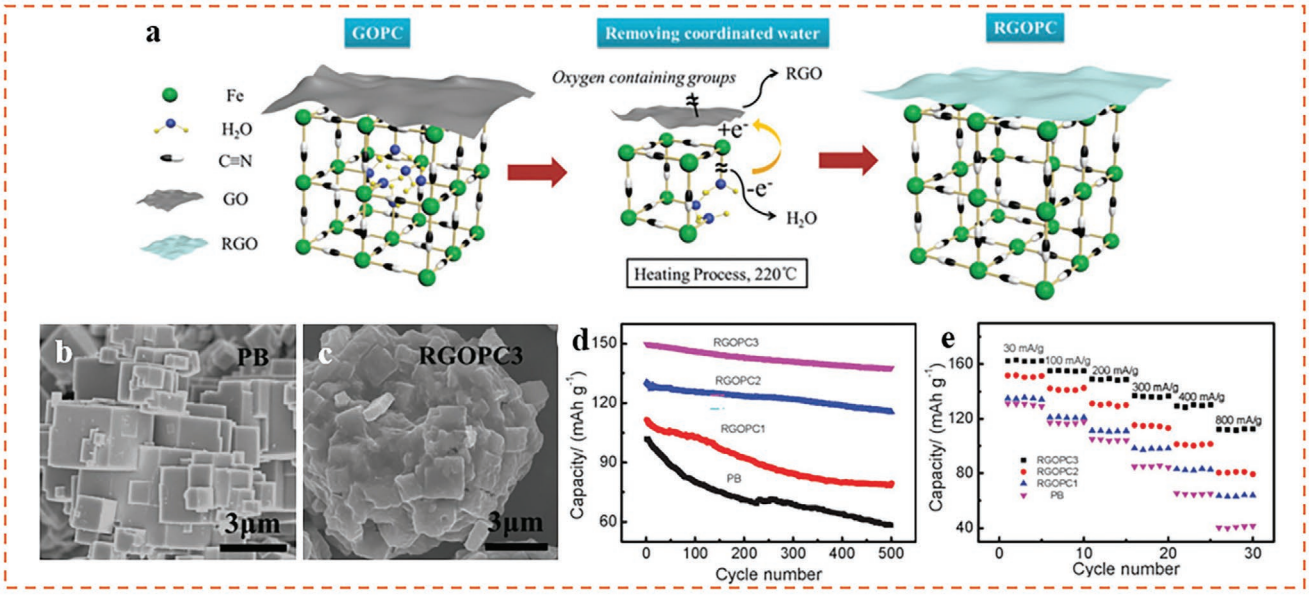

Figure 15. a) schematic mechanism for the removal of coordinated water from RGOPC; SEM images of b) PB and c) RGOPC; comparison of d) cycling performance and e) rate performance. Reproduced with permission.[106] Copyright 2015, Royal Society of Chemistry.

composite was shown in Figure 17b. The charge storage mechanism was adjusted by the combination of capacitive property of MnO_2 and intercalative feature of ZnHCF, and few 2D MnO_2 nanosheets acted as a buffer layer to reduce diffusion controlled limitations to achieve rapid Zn^{2+} ion storage together with sufficient redox reactions. As a result, the ZnHCF@MnO_2 composite exhibited much higher electrode performance than that of the ZnHCF and MnO_2 (Figure 17c–e), with reversible capacity of 118 mAh g^{-1} at 100 mA g^{-1} (75 mAh g^{-1} at 1000 mA g^{-1}) and has good cycling stability.

Zhang et al.[82] reported the truncated CoHCF nanocubes threaded by carbon nanotubes (CoHCF-Cit/CNT) as cathode

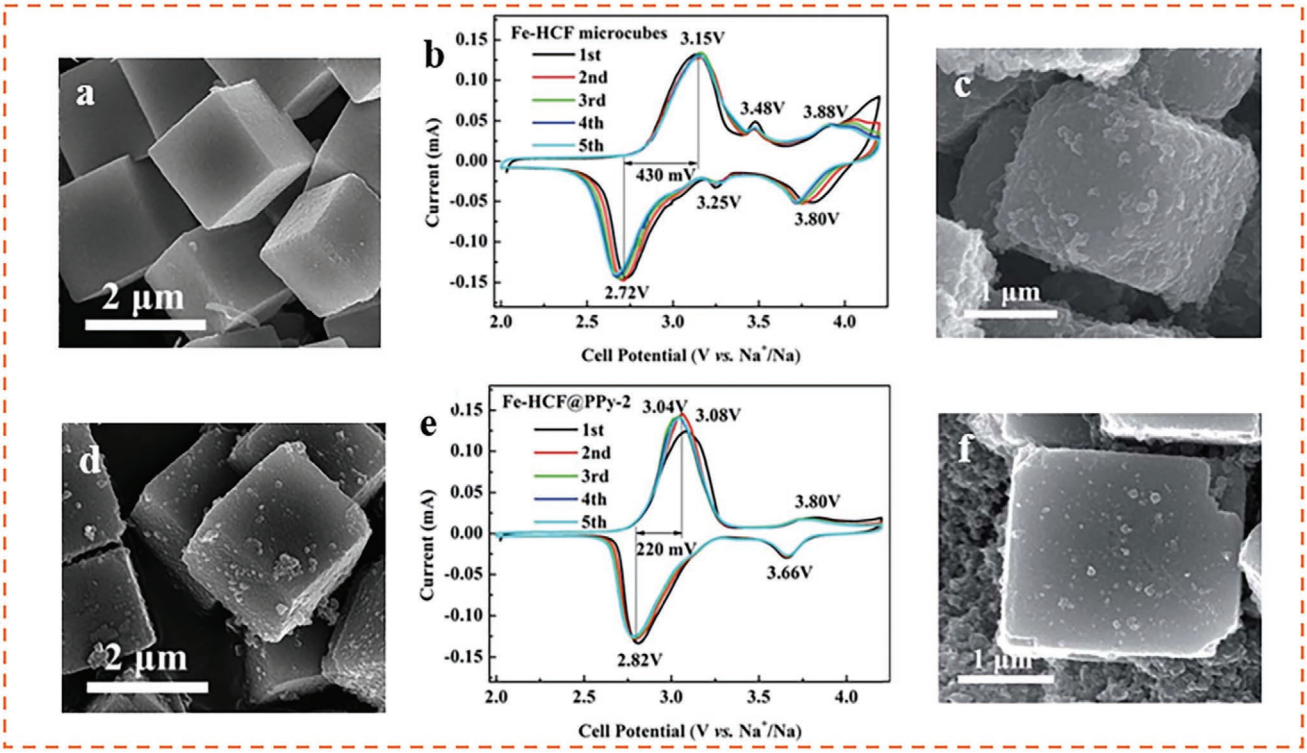

Figure 16. SEM image of pristine a) Fe-HCF and d) Fe-HCF@PPy; CV curves of b) Fe-HCF and e) Fe-HCF@PPy electrodes; SEM image of pristine c) Fe-HCF and f) Fe-HCF@PPy after cycling. Reproduced with permission.[110] Copyright 2016, Royal Society of Chemistry.

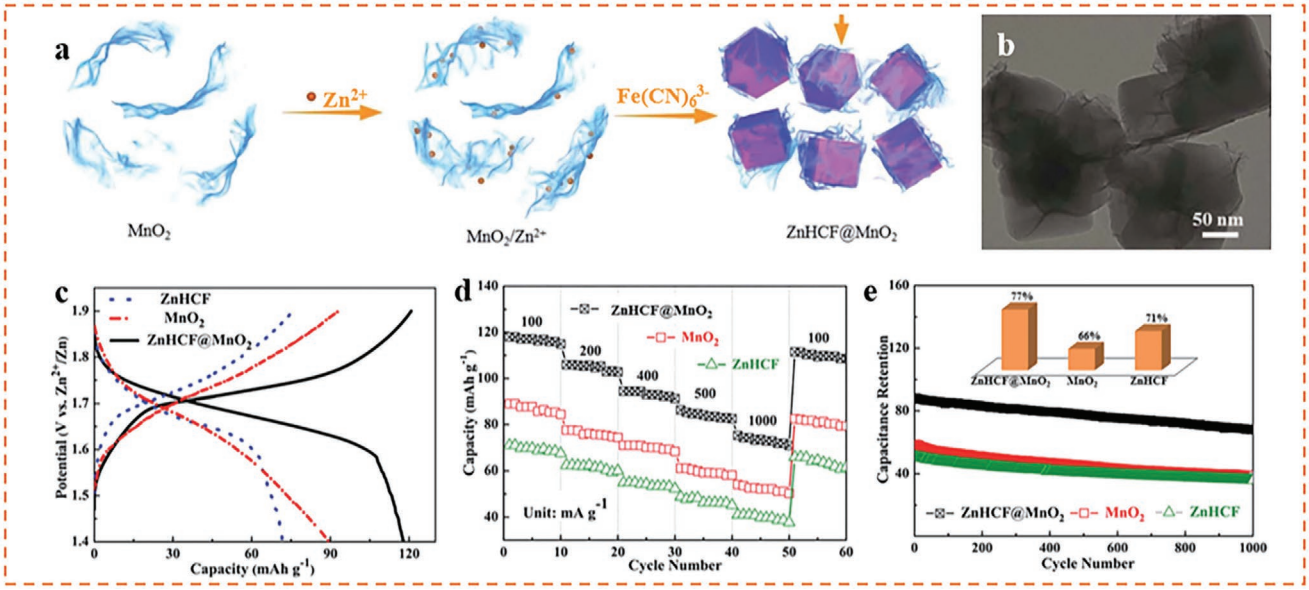

Figure 17. a) Schematic diagram for the fabrication procedures of the ZnHCF@MnO_2 composite, and b) corresponding TEM morphology; comparison of c) capacity, d) rate, and e) cycling performance of ZnHCF, MnO_2, and ZnHCF@MnO_2. Reproduced with permission.[112] Copyright 2017, Royal Society of Chemistry.

in aqueous Na^+/Zn^{2+} dual battery. A facile synthesis process was carried out with citrate and glycerol in the recipe to reduce the reaction rate and the growth rate of CoHCF, and the CNT was treated by concentrated H_2SO_4 and HNO_3 before adding to the electrolyte. The crystal structure of HCF, morphology of Co-HCF and CoHCF-Cit/CNT are shown in **Figure 18**a–c. CNT not only effectively reduce the internal resistance of CoHCF particles, but also can obviously reduce the resistance between adjacent CoHCF particles, as a result, the electrochemical performance of the CoHCF-Cit/CNT was significantly improved (Figure 18d,e), with a high capacity (107.2 mAh g^{-1} at 0.1 A g^{-1}), a high rate performance (68.1 mAh g^{-1} at 5 A g^{-1}), as well as a high cycling stability (capacity retention of 66.6%, over 500 cycle at 1A g^{-1}). In summary, applying PBA-based materials is very

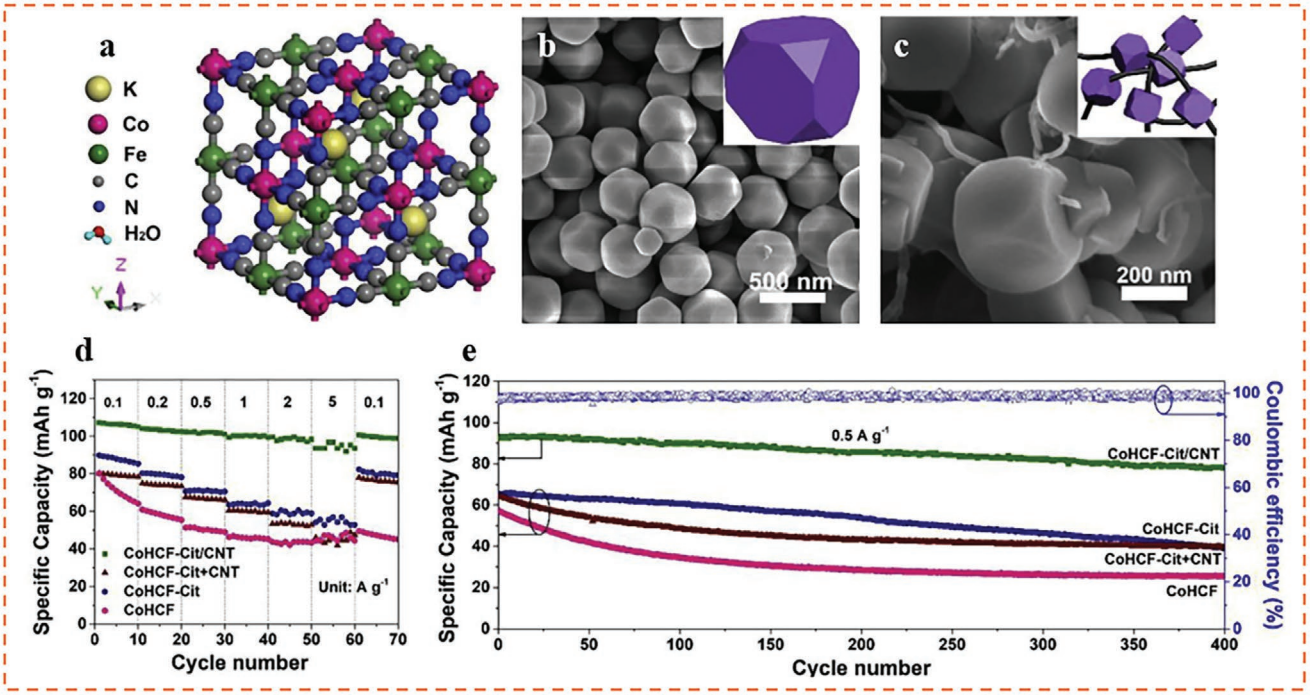

Figure 18. a) crystal simulation of CoHCF; SEM images of b) CoHCF and c) CoHCF-Cit/CNT, comparison of d) rate and e) cycling performance of CoHCF, CoHCF-Cit, CoHCF-Cit+CNT, and CoHCF-Cit/CNT. Reproduced with permission.[82] Copyright 2018, Elsevier.

helpful in enhancing the electrode performance, including enhancing the reversibility of redox reactions, improving the conductivity, suppressing the side reactions, as well as introducing capacitive contributions to the capacity delivery.

5.6. Applying High-Concentration Electrolyte

The side reaction issue in aqueous electrolyte restricts the capacity delivery of PBA electrodes.[113] Due to the limited activated and utilized redox active sites (e.g., Fe^{2+}/Fe^{3+}, Co^{2+}/Co^{3+}, etc.), the PBA-type cathodes usually suffered from ephemeral lifespan and inferior rate capability. Applying high-concentration electrolyte provides a feasible solution for this issue.[114] Yang et al.[80] reported that the high-voltage scanning could be an efficient method to activate the C-coordinated Fe in FeHCF cathode in aqueous 21 M LiTFSI + 1 M $Zn(TFSI)_2$ electrolyte. The $FeFe(CN)_6$ cube (**Figure 19**a) was prepared, and Zn-FeHCF cells were assembled to test the cycling performance. When cycled in the range of (0.5, 1.9) V versus Zn/Zn^{2+}, a rapid capacity loss of up to 58.9% in first 30 charge/discharge cycles was observed, while cycling in range of (0.1, 2.3) V, after an initial drop, the capacity started to steadily increase within 300 cycles (Figure 19b). This result indicated that high-voltage scanning was beneficial to achieve better cycling performance. CV curves showed that the cathodic peaks located at 0.75 V ($C{\equiv}N{-}Fe^{3+/2+}$) decreases rapidly in 10 cycles, while the cathodic peaks located at 1.5 V ($Fe^{3+/2+}{-}C{\equiv}N$) increases gradually in 100 cycles (Figure 19c). The capacity contribution of voltage platform at 1.5 V rapidly increased in the initial 50 cycles and finally contributed 78% of the whole capacity in the 300th cycle (Figure 19d), thus, the voltage platform at 1.5 V dominated the capacity delivery of FeHCF cathode after electrochemical activations. The high-voltage scanning induced activation resulted in an excellent cycling performance of 5000 (82% capacity retention) and 10 000 cycles (73% capacity retention, Figure 19e), as well as a superior rate capability (41 mAh g^{-1} at ≈97C).

Nakamoto et al.[115] also reported a high-voltage sodium-ion battery (over 2 V) using $Na_2MnFe(CN)_6$ as cathode, and $KMnCr(CN)_6$ as anode in 17 M aqueous $NaClO_4$ electrolyte. The highly concentrated electrolyte provided a 2.8 V electrochemical window, which enabled the practical usage of the $Na_2MnFe(CN)_6/KMnCr(CN)_6$ battery. CV curves showed the almost reversible peaks of both $Na_2MnFe(CN)_6$ cathode (Fe^{2+}/Fe^{3+}, Mn^{2+}/Mn^{3+}) and $KMnCr(CN)_6$ anode (Cr^{2+}/Cr^{3+}) (**Figure 20**a). The charge/discharge measurements of both cathode and anode also confirmed their reversible charge/discharge behavior (Figure 20b). The obtained $Na_2MnFe(CN)_6/KMnCr(CN)_6$ battery showed a high voltage and high rate performance, mainly due to the synthetic effect of open-framework electrodes and a highly concentrated but mobile aqueous electrolyte.

Wu et al.[91] reported a reverse dual-ion battery with a nanocomposite having ferrocene encapsulated inside a microporous carbon (Fc/C composite) as anode ($ZnCl_4^{2-}$ insertion), a $Zn_3[Fe(CN)_6]_2$ as cathode (Zn^{2+} insertion) in 30 M $ZnCl_2$ "water-in-salt" electrolyte (**Figure 21**a). By applying high concentrated electrolyte, the dissolution of ferrocene in both Fc/C composite and $Zn_3[Fe(CN)_6]_2$ was depressed, the $ZnCl_4^{2-}$ insertion potential in Fc/C composite anode was depressed, and the cation-insertion potential in the $Zn_3[Fe(CN)_6]_2$ cathode was also raised, thus widening the full cell voltage from 0.6 to 0.95 V (Figure 21b). Consequently, the full cell delivered a reversible capacity of ≈30 mAh g^{-1} based on the total active masses of both the $Zn_3[Fe(CN)_6]_2$ cathode and the Fc/C anode and with an average voltage of ≈0.90 V (Figure 21c), which is obviously superior than that in dilute electrolytes. In summary, applying

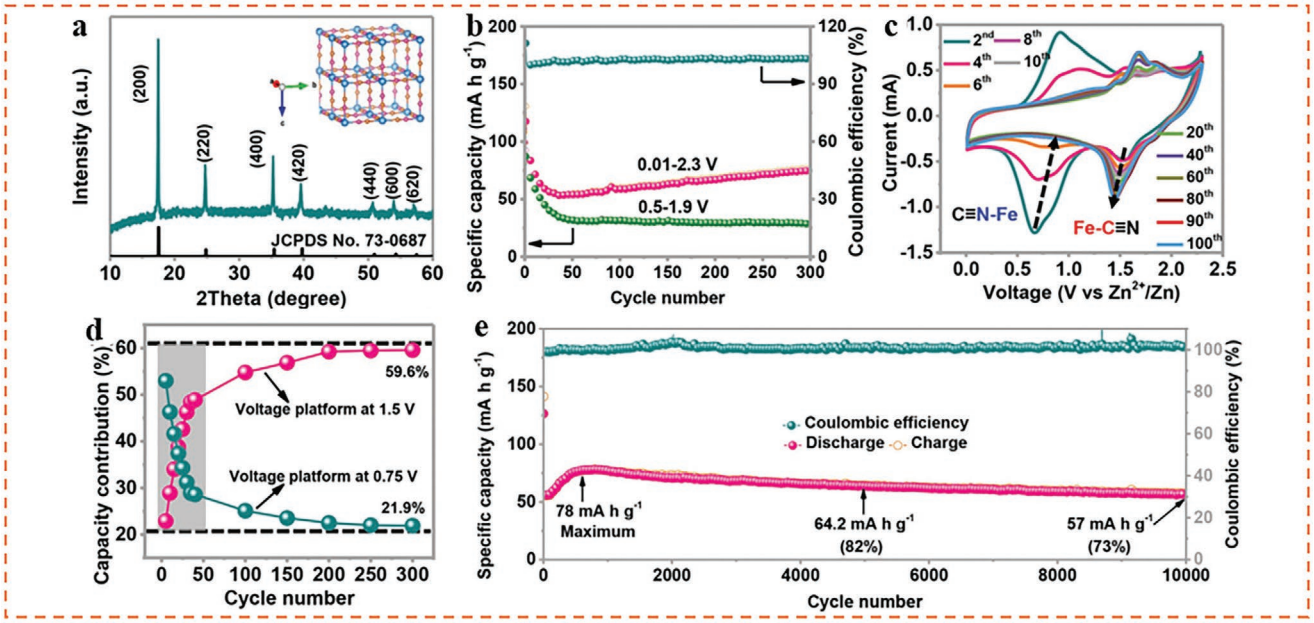

Figure 19. a) XRD pattern and crystal structure of as-prepared FeHCF, b) cycling performance of Zn–FeHCF batteries operated at two different voltage windows, c) in situ CV curves recorded at 2 mV s^{-1}, d) capacity contribution of two voltage platforms after various cycles, e) in-depth discharge/charge process up to 10 000 cycles at 3 A g^{-1}. Reproduced with permission.[80] Copyright 2019, Wiley-VCH.

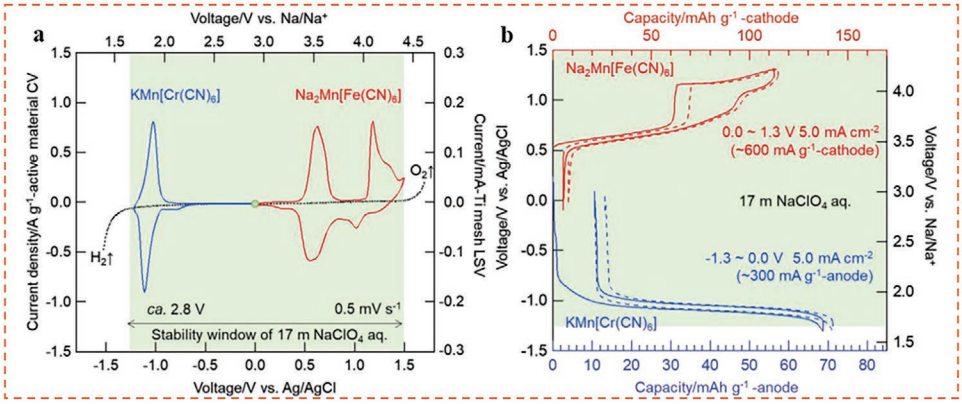

Figure 20. a) CV curves of $Na_2Mn[Fe(CN)_6]$ and $KMn[Cr(CN)_6]$ (colored lines) in 17 m $NaClO_4$ aq. b) charge/discharge curves of $Na_2Mn[Fe(CN)_6]$ and $KMn[Cr(CN)_6]$ half cells. Reproduced with permission.[115] Copyright 2018, Wiley-VCH.

high concentration electrolyte benefits a lot on improving electrochemical window of electrolyte, raising the electrode operating potential, and activating the Fe^{2+}/Fe^{3+}-C redox reactions via high-voltage scanning.

6. Prospects on Future Research and Development of PBA Cathode Materials

In this section, we discuss some prospects on the future development of PBA materials in energy storage/conversion fields. Aiming to achieve advanced electrochemistry, the prospects are focused on the possible applications of PBA electrodes in proton, ammonium-ion, and multivalent batteries, as well as the selection of anode materials and electrolytes for full battery applications. We believe that the following prospects will benefit significantly for the future research and development of PBA materials.

6.1. Application in Proton Batteries

Selecting proton as charge carrier ions inside the Faradaic electrode can achieve an ultra-high rate performance,[116] which is vital for developing the next-generation batteries. Wu et al.[90] reported a Grotthuss proton conduction mechanism in the hydrated PBA cathode, in which proton transfer took place by means of concerted cleavage and formation of O—H bonds in a hydrogen-bonding network. In $Cu[Fe(CN)_6]_{0.63\cdot\Upsilon0.37}\cdot 3.4H_2O$ (CuFe-TBA, **Figure 22**a), where ϒ presented the $[Fe(CN)_6]$ vacancies, the zeolitic water and ligand water in the vacancies formed a hydrogen-bonding "sphere", and the vacancies exist on adjacent sites connected together to build a percolating hydrogen-bonding network, in which the Grotthuss topochemistry could occur. Upon insertion, the protons inserted in CuFe-TBA could first bind with the lattice water molecules to form H_3O^+ (Figure 22b), after relaxation, this proton migrates to a zeolitic water site (Figure 22c), which suggested a lower energy of the zeolitic water site for proton binding. Thus, the proton "migrated" along a water chain via cooperative cleavage and reconnection of the covalent and hydrogen bonds. Under this Grotthuss mechanism, the CuFe-TBA cathode exhibited an ultrahigh rate performance at 4000 C (380 A g^{-1}), and a long cycling life of 0.73 million cycles (Figure 22d,e). When storing Na^+, K^+ or NH_4^+ ions, the CuFe-TBA cathode exhibited much poorer rate performance (Figure 22f), suggesting the intimate correlation between the Grotthuss mechanism and high rate capability of proton storage in CuFe-TBA cathode. The PBA materials provide ideal model frameworks for investing proton storage mechanisms, which is of great importance for developing future high power-density energy storage devices.

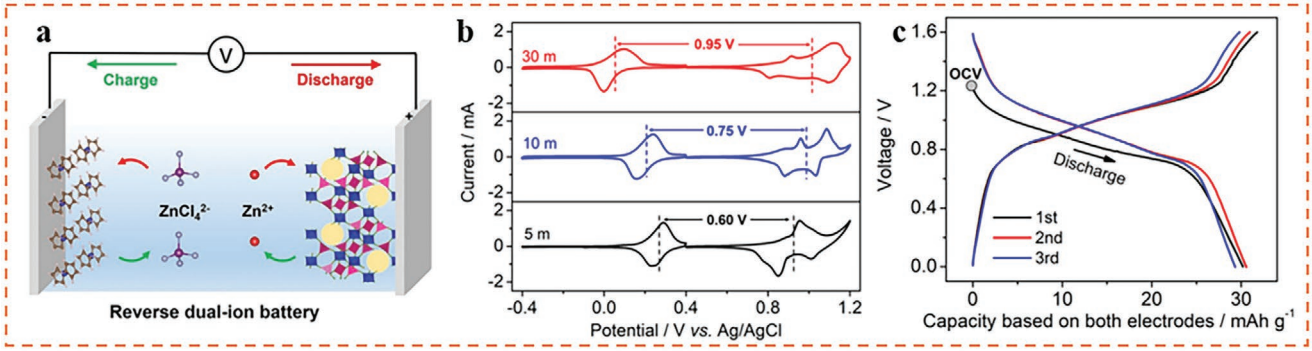

Figure 21. a) Schematic mechanism of the reverse dual-ion battery, b) CV curves of the Fc/C anode and $Zn_3[Fe(CN)_6]_2$ cathode in $ZnCl_2$ electrolytes, c) charge/discharge profiles of the reverse dual-ion full battery at 1 C rate. Reproduced with permission.[91] Copyright 2019, American Chemical Society.

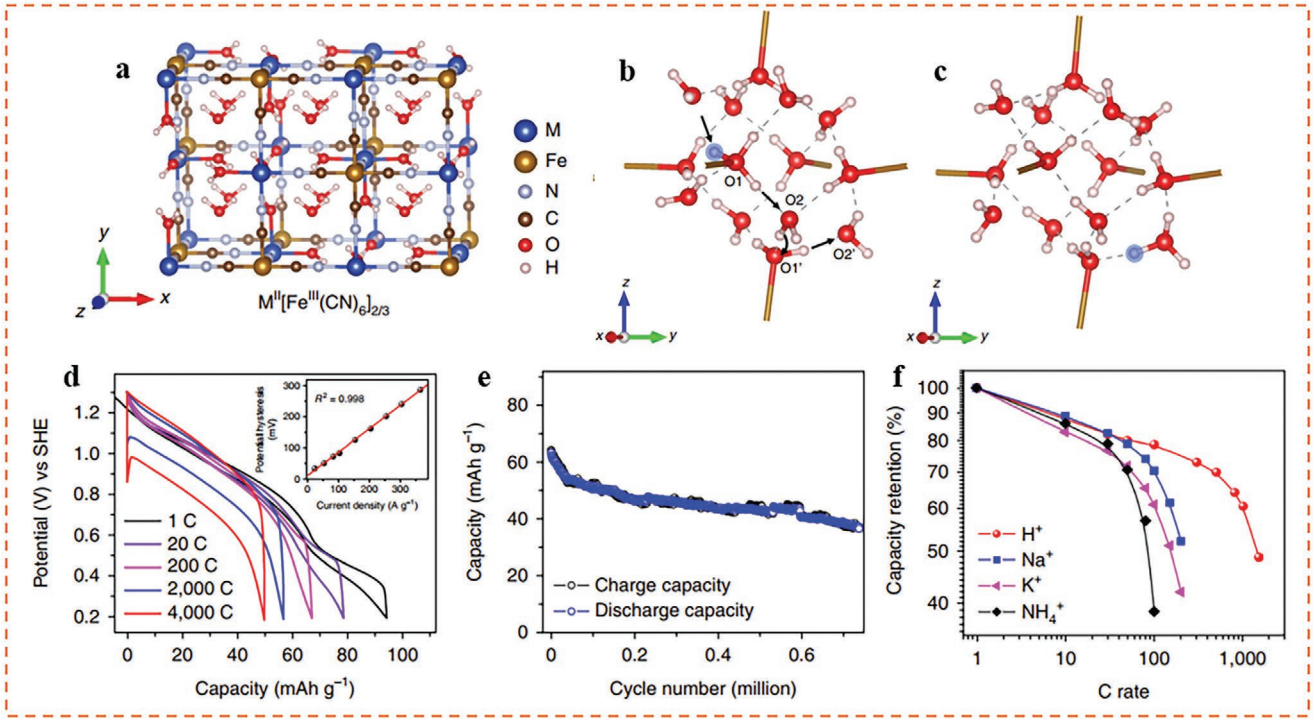

Figure 22. a) Schematic structures CuFe-TBA, A hypothetical ligand hydronium in CuFe-TBA b) before and c) after relaxation, d) Galvanostatic charge/discharge curves at various current rates, e) cycling performance of CuFe-TBA electrodes, f) the rate performance comparison of CuFe-TBA for different cation ions. Reproduced with permission.[90] Copyright 2019, Springer Nature.

Besides, this kind of proton insertion mechanism exists not only in the acidic electrolyte, but also in the mild aqueous electrolytes. The co-intercalation mechanism of H^+ and monovalent/multivalent carrier ions, and corresponding electrochemical behaviors of PBA materials shall be further explored and developed.

6.2. Application in Ammonium Batteries

The intercalation chemistry of NH_4^+ ions in PBA materials has also been disclosed in recent years. Cui's group[117] first reported the NH_4^+ intercalation in Cu-HCF and Ni-HCF comparing with Li^+, Na^+, and K^+ intercalations. Ji's group[118] reported an original "'rocking-chair"' NH_4^+-ion battery comprising $(NH_4)_{1.47}Ni[Fe(CN)_6]_{0.88}$ as the cathode and 3,4,9,10-perylen etetracarboxylic diimide (PTCDI) as anode. They also revealed that the NH_4^+ intercalation/extraction in Berlin green was of nearly zero strain, thus resulting in enhanced cycling stability as compared with that of the Na^+ and K^+ intercalations.[119] Recently, Huang's group also reported the NH_4^+ intercalation in Na-FeHCF[120] and Cu-HCF,[121] they not only achieved excellent cycling and rate performance via controlling morphologies and sizes of Na-FeHCF nanocubes, but also revealed the selective NH_4^+ channel in CuHCF, which leads to high cell voltage (≈1.8 V) and outstanding rate performance of Zn^{2+}/NH_4^+ hybrid batteries. In consideration of the high abundance of NH_4^+ on earth, further investigations shall be done to develop effective PBA cathode materials for NH_4^+ storage, which is of great importance for the development of next-generation batteries.

PBA materials have also been regarded as promising hosts for reversible insertion/extraction of multivalent ions (e.g., Zn^{2+},[49] Mg^{2+},[38] Ca^{2+},[122] Al^{3+}[123,124]), due to their 3D open framework with large interstitial sites for fast reaction kinetics. The robust 3D frameworks of PBAs are stable toward the insertion/extraction of various multivalent ions, and the correlated applications in various kind of batteries could be illustrated as follows:

6.3. Application in Zn-Ion Batteries

Recently, the aqueous Zn-ion batteries has received extensive attention.[49,125] Various kinds of PBA materials have been reported as hosts for Zn^{2+} storage, including ZnHCF,[43] CuHCF,[42] FeHCF,[126] NiHCF,[127] MnHCF,[128] etc. Ma et al.[74] reported the $CoFe(CN)_6$ as host for Zn^{2+} storage, showing excellent electrode performance, which was a pioneering work for Zn-ion battery research field. The $CoFe(CN)_6$ host was prepared via in situ extracting K ion from $KCoFe(CN)_6$, leaving unoccupied interstitial sites for the potential insertion of Zn^{2+}. Thus, a highly operational voltage plateau of 1.75 V (vs Zn/Zn^{2+}), and a high capacity of 173.4 mAh g^{-1} at 0.3 A g^{-1} was obtained, and Co^{2+}/Co^{3+} and Fe^{2+}/Fe^{3+} redox reaction couples accounted for the voltage and capacity delivery. Yang et al.[80] also reported the Li^+/Zn^{2+} hybrid-insertion in FeHCF compound, in which low-spin Fe (Fe—C≡N bonds) redox reaction was activated via high-voltage scanning in a highly concentrated electrolyte, resulting in a record-breaking cycling performance.

6.4. Application in Ca-Ion Batteries

The large ionic radius of Ca^{2+} restricted its application as an intercalating ion for batteries. The Ca^{2+} ion present an ionic radius of ≈118 pm, and the hydrated Ca^{2+} ion in aqueous electrolyte show a large radius of ≈428 pm, which is much larger than that of Li^+, Na^+, and K^+ ions. Selecting suitable host materials is vital for efficient Ca^{2+} insertion/extraction. In 2015, Lipson et al.[41] first reported the concept of reversible Ca^{2+} storage in $Na_{1.1}MnFe(CN)_6$ PBA material. Since then, more PBA materials were investigated as cathode in Ca-ion batteries, including $K_2BaFe(CN)_6$,[129] $K_xMFe(CN)_6$,[130] $MFe(CN)_6$,[131] $K_xFeFe(CN)_6$,[132] etc. The bottleneck of PBA materials as Ca^{2+} ion hosts mainly lies in their poor electrochemical cycling stability, and low capacity delivery, thus, more works need to be done to optimize the electrochemical performance.

6.5. Application in Mg-Ion Batteries

Since Mizuno et al.[37] first reported the Mg^{2+} ion insertion in $K_{0.1}Cu\ [Fe(CN)_6]_{0.7}\cdot 3.6H_2O$, the research on PBAs as hosts for Mg^{2+} ion was widely conducted. Especially, in recent years, PBA materials including $K_{0.86}Ni[Fe(CN)_6]_{0.954}$,[87] $Na_{1.4}Ni_{1.3}Fe(CN)_6$,[133] $Na_2Co[Fe(CN)_6]$,[134] etc., have been investigated as cathodes in aqueous/non aqueous Mg-ion batteries. For instance, Marzak et al.[134] systematically investigated the intercalation of Mg^{2+} ion into the electrodeposited $Na_2Ni[Fe(CN)_6]$, $Na_2Co[Fe(CN)_6]$, $Na_2VO_x[Fe(CN)_6]$, and $NaIn[Fe(CN)_6]$ cathodes, and found that the $NaIn[Fe(CN)_6]$ showed better stability upon repeated Mg^{2+} storage comparing with the other three systems. The authors also revealed that not only the solvation energy of the carrier ions, but also the electronic structure of the electrode materials depending on the nature of the transition metals determined the Mg-ion insertion electrochemistry in the PBA cathodes.

6.6. Application in Al-Ion Batteries

As a trivalent ion, Al^{3+} ion possesses the highest charge density, leading to high electrostatic interaction between the intercalated Al^{3+} and host frameworks, as well as poor diffusion kinetics. In 2015, Liu et al.[39] first reported the reversible Al^{3+} insertion in a CuHCF cathode. Since then, more PBA materials are developed as cathodes for Al^{3+} storage, including $K_2CoFe(CN)_6$,[135] $K_{0.02}Ni_{1.45}[Fe(CN)_6]$,[88] $K_2CoFe(CN)_6$,[135] $FeFe(CN)_6$,[79] etc. For instance, Zhou et al.[79] (in 2019) reported the electrochemical Al^{3+}-ion storage in $FeFe(CN)_6$ cathode using a 5 M $Al(CF_3SO_3)_3$ "water-in-salt" electrolyte (Al-WISE). The Al-WISE presented a wide electrochemical window (2.65 V) and suppressed the dissolution of FeHCF cathode, resulting in a high discharge capacity of 116 mAh g^{-1} and a superior cycle stability >100 cycles. However, the intercalation mechanism of Al^{3+} ions in PBA-based Al-ion cathodes is still elusive, and more works are warranted to decipher the exact mechanism, as well as to seek high-performance anode materials. Nevertheless, PBA materials have provided a standard open-framework structure for investigating the insertion chemistry of multivalent ions. It is crucial to understand the underlying electrochemistry, which could pave the way for the exploration of more advanced PBA materials.

6.7. Screening Suitable Anode Materials and Electrolytes for Practical Applications

The selection of suitable cathode, anode, and electrolyte is the key to the successful usage of a full battery.[136–140] **Table 1** provides some previously reported PBA-based full batteries, including Na-ion, K-ion, Zn-ion, Mg-ion, and Al-ion full batteries. There exist a lot of combinations of anode materials and electrolytes, taking the Na-ion batteries as example, the anode materials can be TiS_2,[84] $NaTi_2(PO_4)_3$,[75] Na foil,[85] FeHCF,[141] and $KMn[Cr(CN)_6]$,[115] etc., and the applied aqueous/non-aqueous electrolytes are selected based on their electrochemical windows. For aqueous Zn-ion batteries, Zn-based anode is promising in future practical applications.[142] Considering the low-cost, high battery performance, and high safety, the aqueous batteries were believed to be promising in future energy storage fields, especially in large-scale energy storage field. We highlight that the aqueous $Na_2Mn[Fe(CN)_6]$ || $KMn[Cr(CN)_6]$,[115] and $CoFe(CN)_6$ || Zn[74] cells are among the most promising next-generation PBA-based full batteries. On the other hand, for the PBA-based full cells with Mg^{2+}-ion, Ca^{2+}-ion, and Al^{3+}-ion insertion chemistry, there is still a long way to go for industrial application, mainly due to the lack of suitable anode materials.

6.8. Summaries and Prospects

Prussian blue analogues have been widely used in electrochemical energy storage because of their low cost, stable open framework, easy preparation, and non-toxicity. In this review, we have made summaries on crystal structures, electrode reactions mechanisms, optimization strategies for high-performance PBA materials, and have also reviewed some possible applications of advanced PBA materials as cathodes for proton, ammonium-ion, and multivalent-ion batteries. For future development of PBA materials in energy storage/conversion fields, some prospects have been outlined as follows:

i) The intrinsic electrochemical performance of PBA materials is strongly affected by the crystal vacancies, which can increase the structural water content, and consequently reduce the redox-active sites. Improving crystallinity is vital for developing high-performance PBA materials. We believe that skillful selection of complexing agents during synthesis process is the most feasible way to optimize the crystallization of PBA materials,[75,143] especially in scale-up manufacture. Furthermore, the poor electrical conductivity of PBA materials is another critical challenge for their commercialization. Mixing with various conductive carbon materials during synthesis process is one of the effective methods to overcome this issue.
ii) The future energy storage devices call for the next-generation PBA materials with higher operating voltage, better rate performance, higher cycling stability, as well as larger capacity delivery. Various optimization strategies will be adapted to

Table 1. Summary of full cell performance (PBA cathode, anode, electrolyte, electrode performance).

Na-ion battery			
Cathode	Anode	Electrolyte	Electrode performance
g-$Ni_{0.1}Mn_{0.9}HCF$[84]	TiS_2	1 M $NaPF_6$ in EC/DMC/FEC	112 mAh g^{-1} at 0.5 C
HQ-NiCoHCF[75]	$NaTi_2(PO_4)_3$	1 M $NaClO_4$ in EC/DEC	125.6 mA h g^{-1} at 15 mA g^{-1}
$Na_xMnFe(CN)_6$[85]	Na foil	1 M $NaClO_4$ in EC/DEC	123 mAh g^{-1} at 10 mA g^{-1}
CuHCF[141]	FeHCF	Aqueous $NaNO_3$ electrolyte	50 mAh g^{-1} with average voltage of ≈0.70 V
$Na_2Mn[Fe(CN)_6]$[115]	$KMn[Cr(CN)_6]$	Aqueous 17 M $NaClO_4$	≈40 mAh g^{-1} with voltage of 1.7 V based on both cathode and anode
K-ion battery			
Cathode	Anode	Electrolyte	Electrode performance
$K_2FeFe(CN)_6$[77]	$NaTi_2(PO_4)_3$	K_2SO_4/Na_2SO_4 mixed aqueous solutions	125 mAh g^{-1} at 0.5 C
Fe-substituted Mn-rich PBA[55]	Organic PTCDI anode	22 M KCF_3SO_3	63 mAh g^{-1} at 0.5 C (based on both cathode and anode), voltage of 1.27 V
Zn-ion battery			
Cathode	Anode	Electrolyte	Electrode performance
ZnHCF[43]	Zn	0.5 M Na_2SO_4, 0.5 M K_2SO_4, 1 M $ZnSO_4$ in H_2O	65.4 mAh g^{-1} at 1C average operating voltage of ≈1.7 V.
$CoFe(CN)_6$[74]	Zn	4 mol $Zn(OTf)_2$ into 1 kg H_2O	171.64 mAh g^{-1} at 0.2 A g^{-1}, average voltage of 1.75 V.
FeHCF[80]	Zn	21 M LiTFSI + 1 M $Zn(TFSI)_2$	76 mAh g^{-1} at 1 A g^{-1}, with average voltage of 1.5 V.
Mg-ion battery			
Cathode	Anode	Electrolyte	Electrode performance
Ni-HCF[133]	Polyimide	1 M $MgSO_4$ in H_2O	38 mAh g^{-1} at a 0.2 A g^{-1} based on PBN/polyimide electrodes
$K_{0.86}Ni[Fe(CN)_6]_{0.954}$[87]	activated carbon	0.5 M $Mg(ClO_4)_2$ in acetonitrile	48.3 mAh g^{-1} at a 0.2 C, average voltage at 2.99 V (vs Mg/Mg^{2+})
Al-ion battery			
Cathode	Anode	Electrolyte	Electrode performance
$K_{0.02}Ni_{1.45}[Fe(CN)_6]$[88]	Al	5 M $Al(OTf)_3$ in H_2O	45 mAh g^{-1} at a 20 mA mg^{-1} based on $K_{0.02}Ni_{1.45}[Fe(CN)_6]$
$Al_{0.2}CuFe–PBA$[40]	activated carbon	$Al(NO_3)_3$ electrolyte	37 mAh g^{-1} at 1C with average voltage of 0.5 V

achieve this goal, including crystal vacancy reduction, metal-substitution, concentration gradient or core–shell structure, novel morphology design, etc. Among these strategies, from our point of view, the metal-substitution provides a fundamental and atomic-level modulation of electrochemical properties of PBA electrodes. We emphasize that composition optimization of PBA materials through a high throughput approach can be a feasible way for selecting high-performance PBA materials.

iii) It is reported that PBA materials show excellent electrochemical performance in aqueous batteries.[45] However, their energy storage mechanism is still under debate. In addition to the traditional intercalation/extraction of charge-carrier ions, the co-intercalation/extraction of protons and metal ions is observed, especially in aqueous Zn-ion batteries.[49] In our opinion, the participation of proton intercalation in PBA materials can lead to better reaction kinetics, which is vital for achieving high power density of aqueous batteries. Therefore, more efforts shall be done on exploring the electrochemical behaviors of PBA materials in aqueous electrolytes.

iv) For intercalation of multivalent ions in PBA-based electrodes, the poor diffusion kinetics are mainly due to the large electrostatic interaction between multivalent ions and host frameworks.[144] It is reported that structural water can accelerate the diffusion of multivalent ions via charge shielding mechanism. However, as discussed above, the existence of structural H_2O in PBA materials can promote crystal vacancy formation, leading to reduced electrode cycle lifespan. Thus, seeking a balance between the content of structural water and the length of cycle lifespan of PBA electrode materials is very important for the development of PBA-based hosts for multivalent ions storage.

v) Further explorations on more advanced synthesis methods are also necessary to achieve higher crystal stability, higher reversibility of redox reactions, better diffusion kinetics of carrier ions, higher ionic/electronic conductivity, improved electrode operating voltage, suppressed side reactions, as well as gaining more capacitive contributions to the electrode capacity delivery. This review provides a comprehensive understanding of PBA materials, and will serve as a guidance for future research and development of PBA materials in energy storage/conversion fields.

Supporting Information

Supporting Information is available from the Wiley Online Library or from the author.

Acknowledgements

H.C.Y. and R.Z.Q. contributed equally to this work. This work was financially supported by Basic and Applied Basic Research Foundation of Guangdong Province (No. 2019A1515110094), Shenzhen Natural Science Foundation (No. JCYJ20190813110605381).

Conflict of Interest

The authors declare no conflict of interest.

Keywords

cathode, energy storage/conversion, Prussian blue analogues, rechargeable batteries

Received: August 17, 2020
Revised: September 23, 2020
Published online: October 9, 2020

[1] Q. Liu, M. Chen, C. Zou, H. Jin, S. Wang, S. Chou, Y. Liu, S. Dou, *Adv. Funct. Mater.* **2020**, *30*, 1909530.
[2] L. Reguera, C. P. Krap, J. Balmaseda, E. Reguera, *J. Phys. Chem. C* **2008**, *112*, 15893.
[3] S. S. Kaye, J. R. Long, *J. Am. Chem. Soc.* **2005**, *127*, 6506.
[4] K. W. Chapman, P. D. Southon, C. L. Weeks, C. J. Kepert, *Chem. Commun.* **2005**, *26*, 3322.
[5] M. Wang, C. Zhuo, L. He, Q. P. Lin, *Chin. J. Struct. Chem.* **2019**, *38*, 345.
[6] Y. Kamachi, M. Zakaria, N. Torad, T. Nakato, T. Ahamad, S. Alshehri, V. Malgras, Y. Yamauchi, *J. Nanosci. Nanotechnol.* **2016**, *16*, 4200.
[7] D. Parajuli, A. Takahashi, H. Noguchi, A. Kitajima, H. Tanaka, M. Takasaki, K. Yoshino, T. Kawamoto, *Chem. Eng. J.* **2016**, *283*, 1322.
[8] T. Chen, Z. Yan, H. Lin, G. Chen, S. Chen, *Chin. J. Struct. Chem.* **2018**, *37*, 2024.
[9] Z. Qin, Y. Li, N. Gu, *Adv. Healthcare Mater.* **2018**, *7*, 1800347.
[10] S. Wang, C. Chen, L. Chen, *Sci. Technol. Adv. Mater.* **2013**, *14*, 10.
[11] A. M. Nasrin Etebari, S. Ali Beyramabadi, *Chin. J. Struct. Chem.* **2018**, *37*, 375.
[12] Z. Tavakoli, *Chin. J. Struct. Chem.* **2019**, *38*, 1421.
[13] A. Karyakin, *Electroanalysis* **2001**, *13*, 813.
[14] A. Karyakin, O. Gitelmacher, E. Karyakina, *Anal. Chem.* **1995**, *67*, 2419.
[15] F. Ricci, G. Palleschi, *Biosens. Bioelectron.* **2005**, *21*, 389.
[16] Z. Wang, J. Hua, Y. Wang, H. Yi, W. Zhao, Q. Zhao, H. Jia, B. Fei, F. Pan, *Small Methods* **2020**, *4*, 2000082.
[17] Z. Wang, L. Han, Z. Wang, H. Wang, Q. Zhao, J. Liu, F. Pan, *Nano Energy* **2019**, *56*, 92.
[18] H. Wang, W. Ge, T. Chen, M. Qu, G. Peng, *Prog. Chem.* **2017**, *29*, 683.
[19] W. Li, G. Cheng, S. Chou, H. Liu, S. Dou, *Small* **2019**, *15*, 1900470.
[20] V. Neff, *J. Electrochem. Soc.* **1978**, *125*, 886.
[21] J. McCargar, V. Neff, *J. Phys. Chem.* **1988**, *92*, 3598.
[22] N. Imanishi, T. Morikawa, J. Kondo, Y. Takeda, O. Yamamoto, N. Kinugasa, T. Yamagishi, *J. Power Sources* **1999**, *79*, 215.
[23] N. Imanishi, T. Morikawa, J. Kondo, R. Yamane, Y. Takeda, O. Yamamoto, H. Sakaebe, M. Tabuchi, *J. Power Sources* **1999**, *81–82*, 530.
[24] A. Eftekhari, *J. Power Sources* **2004**, *126*, 221.
[25] M. Okubo, D. Asakura, Y. Mizuno, J. D. Kim, T. Mizokawa, T. Kudo, I. Honma, *J. Phys. Chem. Lett.* **2010**, *1*, 2063.
[26] A. Paolella, C. Faure, V. Timoshevskii, S. Marras, G. Bertoni, A. Guerfi, A. Vijh, M. Armand, K. Zaghib, *J. Mater. Chem. A* **2017**, *5*, 18919.
[27] C. Wessells, R. Huggins, Y. Cui, *Nat. Commun.* **2011**, *2*, 550.
[28] S. Colin, D. Wessells, R. Huggins, Y. Cui, *Nano Lett.* **2011**, *11*, 5421.
[29] Y. Lu, L. Wang, J. Cheng, J. Goodenough, *Chem. Commun.* **2012**, *48*, 6544.
[30] B. Wang, Y. Han, X. Wang, N. Bahlawane, H. Pan, M. Yan, Y. Jiang, *iScience* **2018**, *3*, 110.
[31] K. Zhang, T. H. Lee, H. Noh, T. Islamoglu, O. Farha, H. Jang, J. Choi, M. Shokouhimehr, *ACS Appl. Mater. Interfaces* **2019**, *11*, 31799.
[32] Z. Song, W. Liu, Q. Zhou, L. Zhang, Z. Zhang, H. Liu, J. Du, J. Chen, G. Liu, Z. Zhao, *J. Power Sources* **2020**, *465*, 228266.
[33] Y. Zhu, P. Chen, Y. Zhou, W. Nie, Y. Xu, *J. Mater. Sci.* **2018**, *53*, 12467.
[34] H. Pang, Y. Zhang, T. Cheng, W. Lai, W. Huang, *Nanoscale* **2015**, *7*, 16012.
[35] L. Zhou, M. Zhang, Y. Wang, Y. Zhu, L. Fu, X. Liu, Y. Wu, W. Huang, *Electrochim. Acta* **2017**, *232*, 106.
[36] Q. Zhao, M. Zhao, J. Qiu, H. Pang, W. Lai, W. Huang, *Inorg. Chem. Front.* **2017**, *4*, 442.
[37] M. Mizuno, E. Hosono, T. Kudo, K. Oh-ishi, A. Okazawa, N. Kojima, R. Kurono, S. Nishimura, A. Yamada, *J. Mater. Chem. A* **2013**, *1*, 13055.
[38] R. Wang, R. Huggins, Y.i Cui, *Nano Lett.* **2013**, *13*, 5748.
[39] S. Liu, G. Pan, G. Li, X. Gao, *J. Mater. Chem. A* **2015**, *3*, 959.
[40] Z. Li, W. Xing, W. Carter, Y. Chiang, *Adv. Energy Mater.* **2015**, *5*, 1401410.
[41] A. Lipson, B. Pan, S. Lapidus, C. Liao, J. Vaughey, B. Ingram, *Chem. Mater.* **2015**, *27*, 8442.
[42] R. Trcoli, F. Mantia, *ChemSusChem* **2015**, *8*, 481.
[43] L. Zhang, X. Zhou, Z. Liu, *Adv. Energy Mater.* **2015**, *5*, 1400930.
[44] J. Huang, Y. Ma, D. Bin, Y. Wang, Y. Xia, *Small Methods* **2019**, *3*, 1800272.
[45] J. Qian, C. Wu, Y. Cao, Z. Ma, Y. Huang, X. Ai, H. Yang, *Adv. Energy Mater.* **2018**, *8*, 1702619.
[46] A. Zhou, W. Cheng, W. Wang, Q. Zhao, J. Xie, W. Zhang, H. Gao, L. Xue, J. Li, *Adv. Energy Mater.* **2020**, 2000943, https://doi.org/10.1002/aenm.202000943.
[47] J. Chen, L. Wei, A. Mahmood, Z. Pei, Z. Zhou, X. Chen, Y. Chen, *Energy Storage Mater.* **2020**, *25*, 585.
[48] Y. Li, K. Yang, B. Cao, Z. Li, L. Yang, F. Pan, *Mater. Today Energy* **2019**, *14*, 100332.
[49] M. Song, H. Tan, D. Chao, H. Fan, *Adv. Funct. Mater.* **2018**, *28*, 1802564.
[50] J. Zheng, Y. Ye, F. Pan, *Natl. Sci. Rev.* **2020**, *7*, 242.
[51] A. Ludi, *Chimia* **1970**, *24*, 445.
[52] H. Buser, W. Fetter, A. Ludi, *Inorg. Chem.* **1977**, *16*, 2704.
[53] F. Herren, P. Fischer, A. Ludi, W. Halg, *Inorg. Chem.* **1980**, *19*, 956.
[54] J. Wu, K. Dai, Z. Zhuo, L. Wray, G. Liu, Z. Shen, R. Zeng, Y. Lu, W. Yang, *J. Am. Chem. Soc.* **2017**, *139*, 18358.
[55] L. Jiang, Y. Lu, C. Zhao, J. Zhao, X. Yu, Y. Hu, *Nat. Energy* **2019**, *4*, 495.
[56] W. Lee, M. Pasta, S. Lee, N. Liu, Y. Cui, *Nat. Commun.* **2014**, *5*, 5280.
[57] J. Song, Y. Lu, J. Liu, B. Guo, P. Xiao, J. Lee, X. Yang, G. Henkelman, J. Goodenough, *J. Am. Chem. Soc.* **2015**, *137*, 2658.
[58] Q. Zhao, S. Ding, A. Song, R. Qin, F. Pan, *Chin. J. Struct. Chem.* **2020**, *39*, 388.
[59] Q. Zhao, X. Chen, Z. Wang, L. Yang, R. Qin, J. Yang, Y. Song, S. Ding, M. Weng, W. Huang, J. Liu, W. Zhao, G. Qian, K. Yang, Y. Cui, H. Chen, F. Pan, *Small* **2019**, *15*, 1904545.
[60] W. Li, C. Han, Y. Wang, H. Liu, *Chin. J. Struct. Chem.* **2020**, *39*, 31.
[61] M. Zhang, Y. Chen, F. Pan, Y. Ren, *Chin. J. Struct. Chem.* **2020**, *39*, 26.
[62] M. Liu, Q. Zhao, H. Liu, J. Yang, L. Y. X. , Y. Cui, W. Huang, W. Zhao, A. Song, Y. Wang, S. Ding, Y. Song, G. Qian, H. Chen, F. Pan, *Nano Energy* **2019**, *64*, 103942.

[63] G. Wang, Z. Guo, K. Niu, J. Lin, *Chin. J. Struct. Chem.* **2020**, *39*, 401.
[64] C. Lin, J. Li, C. Wang, F. Pan, *Chin. J. Struct. Chem.* **2019**, *39*, 2015.
[65] Z. Zhuo, F. Pan, W. Yang, *Chin. J. Struct. Chem.* **2019**, *38*, 2009.
[66] S. Phadke, R. Mysyk, M. Anouti, *J. Energy Chem.* **2020**, *40*, 31.
[67] M. Pasta, R. Wang, R. Ruffo, R. Qiao, H. Lee, B. Shyam, M. Guo, Y. Wang, L. Wray, W. Yang, M. Toney, Y. Cui, *J. Mater. Chem. A* **2016**, *4*, 4211.
[68] B. Xie, L. Wang, J. Shu, X. Zhou, Z. Yu, H. Huo, Y. Ma, X. Cheng, G. Yin, P. Zuo, *ACS Appl. Mater. Interfaces* **2019**, *11*, 46705.
[69] H. Lee, M. Pasta, R. Wang, R. Ruffo, Y. Cui, *Faraday Discuss.* **2014**, *176*, 69.
[70] W. Li, F. Zhang, X. Xiang, X. Zhang, *J. Phys. Chem. C* **2017**, *121*, 27805.
[71] B. He, P. Man, Q. Zhang, C. Wang, Z. Zhou, C. Li, L. Wei, Y. Yao, *Small* **2019**, *15*, 1905115.
[72] Y. Mizuno, M. Okubo, E. Hosono, T. Kudo, H. Zhou, K. Oh-ishi, *J. Phys. Chem. C* **2013**, *117*, 10877.
[73] W. Li, X. Xiang, X. Zhang, *ChemElectroChem* **2018**, *5*, 350.
[74] L. Ma, C. Long, X. Li, Y. Zhao, Z. Liu, Z. Huang, B. Dong, J. Zapien, C. Zhi, *Adv. Energy Mater.* **2019**, *9*, 1902446.
[75] J. Peng, H. Yi, W. Hu, Y. Yu, J. Yin, Y. Shen, Y. Liu, J. Luo, Y. Xu, P. Wei, Y. Li, Y. Jin, Y. Ding, L. Miao, J. Jiang, J. Han, Y. Huang, *Adv. Energy Mater.* **2018**, *8*, 1702856.
[76] J. Wang, C. Mi, P. Nie, S. Dong, S. Tang, X. Zhang, *J. Electroanal. Chem.* **2018**, *818*, 10.
[77] C. Liu, X. Wang, W. Deng, C. Li, J. Chen, M. Xue, R. Li, F. Pan, *Angew. Chem., Int. Ed.* **2018**, *57*, 7046.
[78] D. Su, A. McDonagh, S. Qiao, G. Wang, *Adv. Mater.* **2017**, *29*, 1604007.
[79] A. Zhou, L. Jiang, J. Yue, Y. Tong, Q. Zhang, Z. Lin, B. Liu, C. Wu, L. Suo, Y. Hu, H. Li, L. Chen, *ACS Appl. Mater. Interfaces* **2019**, *11*, 41356.
[80] Q. Yang, Z. Liu, L. Ma, X. Li, D. Fang, S. Chen, S. Zhang, C. Zhi, *Adv. Mater.* **2019**, *31*, 1901521.
[81] L. Ren, J. Wang, H. Liu, M. Shao, B. Wei, *Electrochim. Acta* **2019**, *321*, 134671.
[82] D. Zhang, J. Zhang, H. Mao, J. Yang, Y. Qian, *J. Power Sources* **2018**, *399*, 1.
[83] J. Song, L. Wang, Y. Lu, J. Liu, B. Guo, P. Xiao, J. Lee, X. Yang, G. Henkelman, J. Goodenough, *J. Am. Chem. Soc.* **2015**, *137*, 2658.
[84] P. Hu, W. Peng, B. Wang, D. Xiao, U. Ahuja, J. Réthoré, K. Aifantis, *ACS Energy Lett.* **2020**, *5*, 100.
[85] W. Li, C. Han, W. Wang, Q. Xia, S. Chou, Q. Gu, B. Johannessen, H. Liu, S. Dou, *Adv. Energy Mater.* **2019**, *10*, 1903006.
[86] W. Ren, M. Qin, Z. Zhu, M. Yan, Q. Li, L. Zhang, D. Liu, L. Mai, *Nano Lett.* **2017**, *17*, 4713.
[87] M. Chae, J. Hyoung, M. Jang, H. Lee, S. Hong, *J. Power Sources* **2017**, *363*, 269.
[88] Y. Gao, H. Yang, X. Wang, Y. Bai, N. Zhu, S. Guo, L. Suo, H. Li, H. Xu, C. Wu, *ChemSusChem* **2020**, *13*, 732.
[89] T. Gupta, A. Kim, S. Phadke, S. Biswas, T. Luong, B. Hertzberg, M. Chamoun, K. Lutterodt, D. Steingart, *J. Power Sources* **2016**, *305*, 22.
[90] X. Wu, W. Shin, L. Ma, T. Liu, X. Bi, Y. Yuan, Y. Qi, T. Surta, W. Huang, J. Neuefeind, T. Wu, P. Greaney, J. Lu, X. Ji, *Nat. Energy* **2019**, *4*, 123.
[91] X. Wu, Y. Xu, C. Zhang, D. Leonard, A. Markir, J. Lu, X. Ji, *J. Am. Chem. Soc.* **2019**, *141*, 6338.
[92] M. Huang, J. Meng, Z. Huang, X. Wang, L. Mai, *J. Mater. Chem. A* **2020**, *8*, 6631.
[93] M. Xie, Y. Huang, M. Xu, R. Chen, X. Zhang, L. Li, F. Wu, *J. Power Sources* **2016**, *302*, 7.
[94] X. Wang, H. Zhang, H. Huo, Y. Yan, G. Li, *Chin. J. Struc. Chem.* **2019**, *38*, 117.
[95] Z. Su, J. Liu, M. Li, Y. Zhu, S. Qian, M. Weng, J. Zheng, Y. Zhong, F. Pan, S. Zhang, *Electrochem. Energy Rev.* **2020**, *3*, 286.
[96] L. Guan, G. Luo, Y. Wang, *Chin. J. Struct. Chem.* **2018**, *37*, 1795.
[97] X. Wu, Y. Luo, M. Sun, J. Qian, Y. Cao, X. Ai, H. Yang, *Nano Energy* **2015**, *13*, 117.
[98] W. Li, S. Chou, J. Wang, Y. Kang, J. Wang, Y. Liu, Q. Gu, H. Liu, S. Dou, *Chem. Mater.* **2015**, *27*, 1997.
[99] Y. Liu, Y. Qiao, W. Zhang, Z. Li, X. Ji, L. Miao, L. Yuan, X. Hu, Y. Huang, *Nano Energy* **2015**, *12*, 386.
[100] Q. Zhao, A. Song, S. Ding, R. Qin, Y. Cui, S. Li, F. Pan, *Adv. Mater.* **2020**, 2002450, https://doi.org/10.1002/adma.202002450.
[101] X. Wang, G. Li, H. Wang, Y. Song, D. Liu, Z. Xu, *Chin. J. Struct. Chem.* **2019**, *38*, 629.
[102] H. Yang, H. Cui, J. Wang, X. Chen, *Chin. J. Struct. Chem.* **2019**, *38*, 1164.
[103] J. Yin, Y. Shen, C. Li, C. Fan, S. Sun, Y. Liu, J. Peng, L. Qing, J. Han, *ChemSusChem* **2019**, *12*, 4786.
[104] J. Nai, X. Lou, *Adv. Mater.* **2019**, *31*, 1706825.
[105] M. Hu, S. Furukawa, R. Ohtani, H. Sukegawa, Y. Nemoto, J. Reboul, S. Kitagawa, Y. Yamauchi, *Angew. Chem., Int. Ed.* **2012**, *51*, 984.
[106] D. Yang, J. Xu, X. Liao, H. Wang, Y. He, Z. Ma, *Chem. Commun.* **2015**, *51*, 8181.
[107] J. Zheng, J. Lu, K. Amine, F. Pan, *Nano Energy* **2017**, *33*, 497.
[108] C. Xue, G. Li, C. Gong, W. Guo, J. Huang, *Chin. J. Struct. Chem.* **2018**, *37*, 1916.
[109] L. Yang, K. Yang, J. Zheng, K. Xu, K. Amine, F. Pan, *Chem. Soc. Rev.* **2020**, *49*, 4667.
[110] Y. Tang, W. Zhang, L. Xue, X. Ding, T. Wang, X. Liu, J. Liu, X. Li, Y. Huang, *J. Mater. Chem. A* **2016**, *4*, 6036.
[111] J. You, Y. Guo, Y. Zhao, Z. Ni, R. Guo, *Chin. J. Struct. Chem.* **2018**, *37*, 1440.
[112] K. Lu, B. Song, Y. Zhang, H. Ma, J. Zhang, *J. Mater. Chem. A* **2017**, *5*, 23628.
[113] Q. Zhao, J. Yang, M. Liu, R. Wang, G. Zhang, H. Wang, H. Tang, C. Liu, Z. Mei, H. Chen, F. Pan, *ACS Catal.* **2018**, *8*, 5621.
[114] J. Zheng, T. L. P. , J. Hu, Y. Feng, L. Yang, M. Zhang, Z. Chen, Y. Lin, J. Lu, J. Neuefeind, Y. Ren, K. Amine, L. Wang, K. Xu, F. Pan, *Chem* **2018**, *4*, 1.
[115] K. Nakamoto, Y. Sawada, M. Ito, S. Okada, *Small Methods* **2019**, *3*, 1800220.
[116] B. Li, D. Zhang, J. Fan, T. Feng, L. Li, *Chin. J. Struct. Chem.* **2018**, *37*, 1723.
[117] C. Wessells, S. Peddada, M. McDowell, R. Huggins, Y. Cui, *J. Electrochem. Soc.* **2011**, *159*, A98.
[118] X. Wu, Y. Qi, J. Hong, Z. Li, A. Hernandez, X. Ji, *Angew. Chem., Int. Ed.* **2017**, *56*, 13026 .
[119] X. Wu, Y. Xu, H. Jiang, Z. Wei, J. Hong, A. Hernandez, F. Du, X. Ji, *ACS Appl. Energy Mater.* **2018**, *1*, 3077.
[120] C. Li, W. Yan, S. Liang, P. Wang, J. Wang, L. Fu, Y. Zhu, Y. Chen, Y. Wu, W. Huang, *Nanoscale Horiz.* **2019**, *4*, 991.
[121] C. Li, J. Wu, F. Ma, Y. Chen, L. Fu, Y. Zhu, Y. Zhang, P. Wang, Y. Wu, W. Huang, *ACS Appl. Energy Mater.* **2019**, *2*, 6984.
[122] C. Lee, S. Jeong, *Electrochim. Acta* **2018**, *265*, 430.
[123] V. Verma, S. Kumar, W. Manalastas Jr, R. Satish, M. Srinivasan, *Adv. Sustainable Syst.* **2019**, *3*, 1800111.
[124] R. Wang, B. Shyam, K. Stone, J. Weker, M. Pasta, H. Lee, M. Toney, Y.i Cui, *Adv. Energy Mater.* **2015**, *5*, 1401869.
[125] L. Jiang, Z. Wu, Y. Wang, W. Tian, Z. Yi, C. Cai, Y. Jiang, L. Hu, *ACS Nano* **2019**, *13*, 10376.
[126] Z. Liu, G. Pulletikurthi, F. Endres, *ACS Appl. Mater. Interfaces* **2016**, *8*, 12158.
[127] K. Lu, B. Song, J. Zhang, H. Ma, *J. Power Sources* **2016**, *321*, 257.
[128] Q. Li, K. Ma, G. Yang, C. Wang, *Energy Storage Mater.* **2020**, *29*, 246.

[129] P. Padigi, G. Goncher, D. Evans, R. Solanki, *J. Power Sources* **2015**, *273*, 460.
[130] T. Tojo, Y. Sugiura, R. Inada, Y. Sakurai, *Electrochim. Acta* **2016**, *207*, 22.
[131] T. Shiga, H. Kondo, Y. Kato, M. Inoue, *J. Phys. Chem. C* **2015**, *119*, 27946.
[132] N. Kuperman, P. Padigi, G. Goncher, D. Evans, J. Thiebes, R. Solanki, *J. Power Sources* **2017**, *342*, 414.
[133] L. Chen, L. Bao, X. Dong, D. G. Truhlar, Y. Wang, C. Wang, Y. Xia, *ACS Energy Lett.* **2017**, *2*, 1115.
[134] P. Marzak, M. Kosiahn, J. Yun, A. Bandarenka, *Electrochim. Acta* **2019**, *307*, 157.
[135] Y. Ru, S. Zheng, H. Xue, H. Pang, *Chem. Eng. J.* **2020**, *382*, 122853.
[136] R. Qin, Y. Wang, Q. Zhao, K. Yang, F. Pan, *Chin. J. Struct. Chem.* **2020**, *39*, 605.
[137] J. Xiang, L. Yang, L. Yuan, K. Yuan, Y. Zhang, Y. Huang, J. Lin, F. Pan, Y. Huang, *Joule* **2019**, *3*, 2334.
[138] G. Qian, X. Liao, Y. X. Zhu, F. Pan, X. Chen, Y. Yang, *ACS. Energy Lett.* **2019**, *4*, 690.
[139] Y.-J. Li, J.-H. Zhou, S.-J. Guo, *Chin. J. Struct. Chem.* **2019**, *38*, 1993.
[140] X. Li, Y. Wei, J. Wu, L. Yuan, Y. Huang, *Chin. J. Struct. Chem.* **2019**, *38*, 1999.
[141] B. Wang, X. Wang, C. Liang, M. Yan, Y. Jiang, *ChemElectroChem* **2019**, *6*, 4848.
[142] H. Jia, Z. Wang, B. Tawiah, Y. Wang, C. Chan, B. Fei, F. Pan, *Nano Energy* **2020**, *70*, 104523.
[143] R. Rehman, J. Peng, H. Yi, Y. Shen, J. Yin, C. Li, C. Fang, Q. Li, J. Han, *RSC Adv.* **2020**, *10*, 27033.
[144] M. Park, H. Asl, A. Manthiram, *ACS Energy Lett.* **2020**, *5*, 2367.

Haocong Yi received his B.S. degree from Huazhong University of Science and Technology (HUST, China) in 2018. He is currently a Ph.D. degree candidate under the supervision of Prof. Feng Pan in School of Advanced Materials, Peking University Shenzhen Graduate School, China. His research interests focuses on the aqueous zinc-ion batteries.

Runzhi Qin received his B.S. degree from University of Science and Technology of Beijing (USTB, China) in 2013, and earned Ph.D. degree from the School of Materials Science and technology at USTB in 2019, majoring in the electrochemical corrosion behavior of iron-based alloys, under the supervision of Prof. Minxu Lu. He is now a post-doctor in Prof. Feng Pan's group in School of Advanced Materials, Peking University Shenzhen Graduate School, China. His research interests mainly focuses on the key materials and technologies for zinc-based batteries.

Shouxiang Ding graduated from South China University of Technology (SUCT, China) and received his B.S. degree from the School of Chemistry and Chemical Engineering in 2019. He is currently a postgraduate student in Prof. Feng Pan's group at the School of Advanced Materials, Peking University Shenzhen Graduate School. His research interests focuses on developing cathode materials for aqueous zinc-ion batteries.

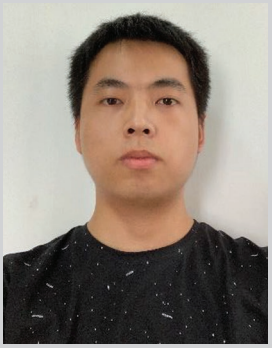

Yuetao Wang graduated from Peking University (PKU, China) and received his Bachelor's Degree from the College of Chemistry and Molecular Engineering in 2018. He is now studying for a Ph.D. degree under the leadership of Prof. Feng Pan at the School of Advanced Materials, Peking University Shenzhen Graduate School, China. He mainly focuses on the research of aqueous zinc-ion battery systems, especially on the vanadium-based cathode materials and the protection of zinc anode.

Shunning Li received his B.E. degree in 2013 and Ph.D. degree in 2018 from School of Materials Science and Engineering, Tsinghua University, China. Currently, he is a postdoc in the group of Prof. Feng Pan at the School of Advanced Materials, Peking University, Shenzhen Graduate School, China. His research interest focuses on the first-principles design of energy storage materials and heterogeneous catalysts.

Qinghe Zhao received his B.S. degree from University of Science and Technology of Beijing (USTB, China) in 2010, and earned Ph.D. degree from the School of Advanced Materials at USTB in 2016, majoring in the electrochemical corrosion behavior of iron-based alloys, under the supervision of Prof. Minxu Lu. He is now an associate researcher in School of Advanced Materials, Peking University Shenzhen Graduate School, China. His research interests mainly focuses on the key materials and technologies for energy storage and conversion applications, including electro-catalyst, zinc ion, and sodium-ion batteries.

Feng Pan, Chair-Professor, Founding Dean of School of Advanced Materials, Peking University, Shenzhen Graduate School, Director of National Center of Electric Vehicle Power Battery and Materials for International Research, received his B.S. degree from the Department of Chemistry, Peking University in 1985 and Ph.D. from Department of P&A Chemistry, University of Strathclyde, UK. He has been engaged in fundamental research on structural chemistry, exploring "Material Gene" for Li-ion batteries, and developing novel energy conversion-storage materials and devices.